Silver nanoparticles synthesis in microfluidic and well-mixed reactors

Pico, Paula; Nathanael, Konstantia; Lavino, Alessio D.; Kovalchuk, Nina M.; Simmons, Mark J.H.; Matar, Omar K.

DOI:
10.1016/j.cej.2023.145692

Chemical Engineering Journal 474 (2023) 145692

Contents lists available at ScienceDirect

Chemical Engineering Journal

journal homepage: www.elsevier.com/locate/cej

Silver nanoparticles synthesis in microfluidic and well-mixed reactors: A combined experimental and PBM-CFD study

Paula Pico [a], Konstantia Nathanael [b,*], Alessio D. Lavino [a], Nina M. Kovalchuk [b], Mark J.H. Simmons [b], Omar K. Matar [a]

[a] Department of Chemical Engineering, Imperial College London, South Kensington Campus, London SW7 2AZ, United Kingdom
[b] School of Chemical Engineering, University of Birmingham, B15 2TT, United Kingdom

ARTICLE INFO

Keywords:
AgNPs
Microfluidic synthesis
PBM-CFD
Residence times
Finke–Watzky two-step mechanism

ABSTRACT

We investigate the production of silver nanoparticles (AgNPs) under different operating conditions of pH, inlet flow rates, and reactants concentration via a combination of population balance modelling and computational fluid dynamics (PBM-CFD) to elucidate our experimental observations in a well-mixed batch reactor and a T-junction microfluidic device. The synthesis process considered herein is based on a reduction protocol involving silver nitrate as precursor and a mixture of tannic acid/trisodium citrate as reducing/stabilising agents. Our novel PBM-CFD framework expands the current kinetic models developed for well-mixed reactors to explicitly account for the spatio-temporal dependence of mixing dynamics for microfluidic reacting flows in order to predict the final particle size distribution of the produced AgNPs. Nucleation and growth models are based on the Finke–Watzky (F–W) two-step mechanism and are directly coupled to the reduction reaction kinetics and the convection–diffusion equations of each species. The T-junction results suggest that the higher residence times involved in operations with lower flow rates are responsible for a cascade of kinetic/reactive and hydrodynamic events, unveiled by our simulations, that lead to higher outlet particle sizes and volume fraction of the particles in the dispersion. The simulation results also provide a characterisation of the radial heterogeneous concentration of particles and particle sizes across the channel typical of continuous-flow microfluidics. Limitations and advantages of our novel modelling approach are discussed in the context of future lines of research.

1. Introduction

Silver nanoparticles (AgNPs) have gained considerable academic and industrial importance over the past two decades as a result of their unique physicochemical properties, which make them suitable for a broad range of applications. Examples of these include but are not limited to, food preservation [4], coating for localised drug delivery [5], fabrication of sterile textiles [6], water disinfection [7], treatment of specific fungal and viral infections [8], surface-enhanced Raman scattering (SERS) [9], and catalysis of organic reactions [10]. The successful usage of AgNPs in a large portion of the aforementioned fields is critically linked to a highly-controlled and reliable fabrication process capable of rapidly synthesising nanoparticles (NPs) of a given size and shape while also minimising polydispersity, reagents consumption, and environmental impact [11].

Microfluidic-based methods have emerged as a promising alternative to traditional large-scale, batch-like systems for the synthesis of NPs. These miniaturised versions of large continuous-flow reactors have proven successful in the synthesis of numerous types of NPs, including gold [12], cadmium sulfide [13], cadmium selenide [14], silica [15], liposomes [16], and indeed, Ag [17], among others. On account of their small working volumes ($O(10^{-12})$ - $O(10^{-6})$ L), and spatial scales ($O(10^{1})$ - $O(10^{2})$ μm) [18], microfluidic channels allow for a high throughput operation under precisely-controlled hydrodynamic conditions, low reagents and energy requirements, high reaction yields, and reduced generation of waste products [19]. Depending on the operation mode, microfluidics are well-known to also induce higher rates of heat and mass transfer in the system [20].

The synthesis of AgNPs via chemical reduction is a well-documented process in the literature and consists of three major steps: (i) reduction of silver ions in solution, Ag^{+}, from a precursor into silver atoms, Ag^{0}, by a reducing agent; (ii) nucleation of AgNPs of a given critical size; and (iii) growth and stabilisation of the NPs through surface-active stabilising/capping agents via steric or electrostatic mechanisms (see schematic of Fig. 1(a)). A substantial amount of experimental and

* Corresponding author.
E-mail address: cxn782@student.bham.ac.uk (K. Nathanael).

https://doi.org/10.1016/j.cej.2023.145692
Received 20 May 2023; Received in revised form 3 August 2023; Accepted 26 August 2023
Available online 30 August 2023

Nomenclature

When shown in equations and general text, Roman or Greek cursive letters represent scalars and bold straight low- ercase Roman letters represent vectors. Dimensionless vari- ables are represented with a tilde.

Abbreviations and roman symbols

AgNPs	Silver nanoparticles
CFD	Computational fluid dynamics
CFL	Courant–Friedrichs–Lewy
F − −W	Finke–Watzky two-step mechanism
ID	Internal diameter
IrNPs	Iridium nanoparticles
LHS	Left-hand side
NDF	Number density function
NP	Nanoparticle(s)
PBE	Population balance equation
PBM	Population balance model
PISO	Pressure-Implicit-of-Split-Operations
PTFE	Polytetrafluoroethylene
QBMM	Quadrature-based moments method
QMOM	Quadrature method of moments
RHS	Right-hand side
RMSE	Root-mean-square error
SAXS	small-angle X-ray
SI	Supporting information
SN	Silver nitrate
TA	Tannic acid
TC	Trisodium citrate
A	Precursor species in the well-mixed reactor
$Ag_{(l)}$	Reduced silver atoms in the T-junction reactor
$Ag_{(s)}$	Silver nuclei species in the T-junction reactor
$Ag_{(s2)}$	Silver NPs species in the T-junction reactor
B	Precursor species in the NPs in the well-mixed reactor
$\mathcal{B}(L_i)^{agg}$	Birth rate of particle size L_i due to agglomeration
C	Reporter species in the well-mixed reactor
Co	Convective courant number
Cv	Coefficient of variation of the distribution
D	Mass diffusivity coefficient in the mixture
d	Average diameter of the distribution
$\mathcal{D}(L_i)^{agg}$	Death rate of particle size L_i due to agglomeration
D_0	Reduced particle diffusivity, according to the Stokes-Einstein expression
d_{crit}	Homogeneous critical nuclei diameter
d_L	Length-based average particle diameter
d_m	Atomic diameter
d_V	Volume-based average particle diameter
Da	Damköhler number
E	T-junction channel diameter
f	Number density function
G	Growth rate
H	T-junction channel length
J	Nucleation rate
k	Kinetic constant
k_B	Boltzmann constant
k_V	Volumetric shape factor
L	Particle size
L_i	Abscissa of the quadrature approximation
L_0	Small non-zero term introduced to close the diffusive term modelled through the Stokes-Einstein expression in the PBE [1]
L_{F--W}	Average particle diameter, as derived by Watzky et al. [2]
m_k	kth order moment of the PSD
MW	Molecular weight
N	Number of nodes in the quadrature approximation
$\mathbf{n}$	Normal unit vector
N_{av}	Avogadro number
p	Pressure
PDI	Polydispersity index
Pe	Péclet number
Q	Volumetric flow rate of either channel inlet in the T-junction
R	Reducing agent species in the T-junction reactor
$\dot{r}$	Rate of reaction
R^2	Coefficient of determination
Re	Reynolds number
S_j	Mass-based source term in the convection–diffusion–reaction conservation equation of species j
St	Stokes number
T	Temperature
t	Time
Δt	Simulation time-step
$\mathbf{u}$	Velocity vector
V	Particle volume
W	Channel inlet length in the T-junction
w	Weight of the quadrature
$\Delta\mathbf{x}$	Mesh size
$\mathbf{x}$	Vector of spatial coordinates
y	Mass fraction

Greek symbols

β_{Br}	Brownian aggregation kernel
δ	Dirac delta function
μ	Viscosity
∇	Gradient operator
ν	Stoichiometric coefficient
ϕ	Volume fraction

computational work has been conducted to illustrate the influence of the chemical nature of the reagents, particularly of the reducing [21] and stabilising agents [22], and the reaction conditions on the final properties of the NPs and their viability for industrial operations. Among many findings, it has been reported that the main predictors of average particle size correspond to the redox potential of the reducing agent, initial concentration and functional groups of the precursor, pH, temperature, and surface-selective affinity of the stabiliser when interacting with the NPs. Specifically, the attainment of small particle sizes has been typically associated with higher precursor concentrations

ρ	Density
σ	Standard deviation of the distribution
ξ	Mixture fraction

Subscripts

0	Initial in the well-mixed reactor
$1, nuc$	Nucleation
$2, g$	Growth
agg	Agglomeration, referring to the characteristic time-scale of particle agglomeration
c	Continuous phase
d	Disperse phase
$diff$	Diffusion, referring to the characteristic time-scale of particle diffusion
f	Final in the well-mixed reactor
i	ith node of the quadrature
ind	Induction, referring to the induction time
$inlet$	Inlet in the T-junction microchannel
j	jth species in the mixture or 'jerk', referring to the induction time calculated by the 'jerk' method in the well-mixed reactor [3]
max	Maximum, referring to the time at which the highest rate of production of B is seen in the well-mixed reactor [3]
min	Minimum
mix	Mixing, referring to the characteristic time-scale of diffusive mixing
num	Numerical, referring to numerical diffusion
p	Piecewise, referring to the induction time calculated by the piecewise method in the well-mixed reactor [3]
$plateau$	Plateau, referring to the time when the precursor has been fully consumed in the well-mixed reactor
R	Reducing agent
r	Reduction reaction
res	Residence, referring to the residence time-scale in the T-junction reactor
rxn	Index indicating a chemical reaction
SN	Silver nitrate
$total$	Total
$trav$	Transversal

(above a certain threshold, which corresponds to 500 ppm according to Sobczak-Kupiec et al. [23]) and higher redox potentials [24], temperatures [25], and pH [26]. It should be noted, however, that the effect of pH has been reported to be reactant-specific. For a comprehensive account of the extensive efforts undertaken to elucidate how particle size and shape are influenced by reaction-related parameters, we refer the reader to Nathanael et al. [27].

One of the very first mechanistic and phenomenological explorations of the chemical synthesis of transition-metal NPs was provided in the breakthrough work of Watzky and Finke [28], where the *Finke–Watzky* (F–W) *two-step mechanism* is first introduced. The F–W mechanism is based on a slow and continuous pseudo-first-order nucleation process (Eq. (1)) followed by an autocatalytic, pseudo elementary growth reaction (Eq. (2)). The nucleation step combines all processes leading up to the appearance of the first NP nucleus, including the chemical reduction of the precursor, A.

$$Nucleation: A \xrightarrow{k_1} B; \quad \dot{r}_1 = k_1[A], \tag{1}$$

$$Growth: A + B \xrightarrow{k_2} 2B; \quad \dot{r}_2 = k_2[A][B], \tag{2}$$

where B represents the NPs and $[\cdot]$ indicates the molar concentration of each species; k_1 and k_2 are the kinetic constants governing nucleation and growth, respectively. From these expressions, and assuming that all of A is consumed into B ($[B] = [A]_0 - [A]$, $[A]_0$ being the initial concentration of A), the temporal evolution of $[A]$ and $[B]$ is given by the expressions of Eq. (3):

$$-\frac{\mathrm{d}[A]}{\mathrm{d}t} = \frac{\mathrm{d}[B]}{\mathrm{d}t} = k_1[A] + k_2[A][B] = k_1[A] + k_2[A]([A]_0 - [A]). \tag{3}$$

The assumptions of the F–W two-step mechanism, manifested in the above equations, have deep implications on the understanding of the underlying dynamics of NP synthesis and on the general applicability of the model to various scenarios. Crucially, in the original F–W mechanism, it is presumed that the growth step is kinetically limited by the incorporation (or 'reaction') of new material into (with) an existing NP and not by the spatial diffusion of this material to reach an available reacting site (i.e., very fast mixing rates are imposed in the system). Multiple experimental [29,30] and modelling [31,32] investigations involving systems under fast mixing conditions for colloidal NPs are found in the literature, confirming the reaction-limited growth. Additional assumptions include a proportional relationship between the growth rate and material concentration in the NPs (Eq. (2)), implying the availability of the entire NP domain (entire particle volume) as a reacting site instead of the surface area only [33], and the generation of NP nuclei directly from the precursor, eliminating the explicit dependence on reduction- and reducing agent-related phenomena.

The features of F–W stand in opposition to other classic mechanisms, including LaMer [34] and Ostwald ripening [35]. Notably, the continuous nucleation and reaction-limited growth of F–W contradict the pulse-like appearance of NP nuclei and diffusion-controlled particle growth of LaMer and supersaturation-driven process of Ostwald ripening [31]. In F–W, the attainment of uniform-sized NPs (despite a continuous nucleation process that constantly adds small-sized nuclei to the dispersion) is explained by assuming that the system adheres to a significantly longer (by approximately two orders of magnitude) nucleation step than growth; this large kinetic disparity separates nucleation from growth.

In a closed and perfectly-mixed system, the F–W mechanism predicts a long induction time – originally envisaged as proportional to $1/k_1$ [28] and later proved to be proportional to $\ln(k_2[A]_0/k_1)/(k_1 + k_2[A]_0)$ [3] – that precedes a fast sigmoidal precursor consumption. For the duration of induction, the precursor concentration remains essentially constant while nucleation takes place. A plot of a typical temporal evolution of the precursor concentration, as proposed in F–W, is depicted in Fig. 1(b), and its mathematical description is given by [28]:

$$[A] = \frac{[A]_0 + k_1/k_2}{1 + (k_1/k_2[A]_0)\exp(t(k_1 + k_2[A]_0))}, \tag{4}$$

which, under the assumptions $k_2[A]_0/k_1 \gg 1$ and $[A] < [A]_0$, transforms into its well-known linearised form:

$$\ln\left(\frac{[A]_0 - [A]}{[A]}\right) = \ln\left(\frac{k_1}{k_2[A]_0}\right) + k_2[A]_0 t. \tag{5}$$

By assuming fully spherical particles, complete separation of nucleation and growth (i.e, the number of nuclei will not change after the induction period is finalised), and equally-sized nuclei, Watzky et al. [2] proposed a simple F–W-based expression for the temporal evolution of *average* particle size after the induction time, t_{ind} (Eq. (6)). Explicit analytic formulas for t_{ind} (Eqs. (7)–(8)), the time at the maximum rate of consumption/production, t_{max} (Eq. (9)), and the time at which the plateau (or full consumption) stage is reached, $t_{plateau}$

(Eq. (10)), were derived by Bentea et al. [3] from the F–W rates of consumption/production (Eq. (3)):

$$L_{F-W} = L_{F-W,f}\left(\frac{[A]_0 - [A]}{[A]_0}\right)^{1/3} \quad (t \geq t_{ind}), \tag{6}$$

$$t_{ind,j} = \frac{\ln\left(\left(2-\sqrt{3}\right)\frac{k_2[A]_0}{k_1}\right)}{k_1 + k_2[A]_0}, \tag{7}$$

$$t_{ind,p} = \frac{k_1 + k_2[A]_0}{(k_1 - k_2[A]_0)^2}\ln\left(\frac{k_2[A]_0}{k_1}\right) + \frac{2}{k_1 - k_2[A]_0}, \tag{8}$$

$$t_{max} = \frac{\ln\left(\frac{k_2[A]_0}{k_1}\right)}{k_1 + k_2[A]_0}, \tag{9}$$

$$t_{plateau} = \frac{\ln\left((2+\sqrt{3})\frac{k_2[A]_0}{k_1}\right)}{k_1 + k_2[A]_0}, \tag{10}$$

where $L_{F-W,f}$ represents particle size after full precursor consumption, intended to be measured experimentally; $t_{ind,j}$ and $t_{ind,p}$ account for slightly different interpretations of the induction time, the former being defined as the point of maximum acceleration in the consumption of $[B]$ ($d^3[B]/dt^3 = 0$) and the latter as the intersection between the tangents at the initial and maximum $d[B]/dt$ points (see Bentea et al. [3] for their full derivation and detailed differences).

The F–W two-step mechanism has been proven highly successful in explaining the experimentally-observed fast precursor consumption that follows an induction period in a diverse array of systems (see Handwerk et al. [31] and references therein), including the synthesis of Ir, Au, and AgNPs under different reducing and stabilising agent conditions (refer to Nathanael et al. [27] for a compilation of typical values of k_1 and k_2 for AgNPs). Nevertheless, the applicability of this model, at least in its original form, to predict the intricacies of particle size and particle size distribution (PSD) is still under debate and we aim to elucidate this in the present work. As will become apparent in the following paragraphs, the exact reason for the inapplicability of F–W to accurately capture all the intricacies related to PSD, as well as potential enhancing adjustments to the model, are highly contested topics in the literature, where multiple, and often contradicting, assertions are made. The work of Perala and Kumar [33] assessed the performance of F–W in the context of IrNPs through a population balance framework. This work presented evidence to suggest that, while the closure parameters of the model can be optimised to fit the experimental mean particle size of Watzky et al. [2], it considerably over-predicts the standard deviation of the PSD (up to approximately 150%). The authors proposed and tested a few variations to the original F–W mechanism, including the growth term dependence on particles surface area instead of their volume, implementation of a reduction reaction to delay the onset of nucleation, a higher-order nucleation dependence on species concentration, and a nucleation expression derived from classical nucleation theory. They showed that the NPs nuclei formation, though slow, artificially increases the size polydispersity, especially when growth is much faster than nucleation.

Handwerk et al. [31,36] and collaborators provided an alternative interpretation of the limited applicability of F–W for estimating the PSD based on a mechanism-enabled population balance model. The model relies on the assumption that monodisperse particles can be obtained in a continuous-nucleation environment if the nucleated particles grow at a faster rate than the larger particles. Based on this, the authors proposed an extension of F–W to a 3-step mechanism given by: $A \xrightarrow{k_1} B$, $A+B \xrightarrow{k_2} C$, and $A+C \xrightarrow{k_3} 1.5C$, where B represents the small-sized nuclei and C the larger particles ($k_2 > k_3$). The authors report a satisfactory agreement between the experimental and numerical evolution of the PSD for IrNPs with their 3-step model while also maintaining the excellent predictions of precursor concentration of the original model.

Mozaffari et al. [30], on the other hand, suggested that ligand activity and their binding to the NPs' surface predominately govern both nucleation and growth in the synthesis of PdNPs. In their PBM and experimental study, the authors devised a growth expression directly dependent on the number of free binding sites per unit area, translating into a growth suppression (enhancement) of the larger (smaller) particles and thus a monodisperse sample within the framework of continuous nucleation.

Continuous-flow synthesis in microfluidic devices, where the reagents involved are not fully mixed at the onset of the process and considerable spatial- and phase-dependent dynamics arise, poses additional challenges to the development of suitable kinetic models to predict the PSD. Recent progress has been made in the estimation of the PSD of NPs synthesised via microfluidics and other continuous-flow channels, including SiO_2 [37,38], CdSe [39], and ibuprofen [40] NPs. These investigations have elucidated the critical role of the system's hydrodynamics on the temporal progression of the system, and how the interplay between reactants' diffusion and residence times, phase interactions, and reaction kinetics greatly influences the PSD. For instance, the experimental campaign and simulations of Bal and Bandyopadhyaya [37] revealed a dominant role of laminar shear and particle–particle chemical interactions on the agglomeration of colliding NPs in a low Reynolds ($Re \sim 2.54$) microfluidic operation. The PBM-CFD numerical results of Kumar and Ganesan [39] have uncovered a substantial heterogeneity in the distribution of the nucleation/growth rates and size polydispersity along the main axis of the microchannel . Crucially, the aforementioned investigations correspond to crystallisation and precipitation processes, which are well-known to be supersaturation-driven events [41]. As detailed previously, the synthesis of AgNPs is completely incompatible with these premises as it is a reduction-driven process under low saturation conditions.

To the best of the authors' knowledge, Liu et al. [42] is the only attempt to explicitly model a reduction-based NP synthesis in microfluidic devices. This work carried out a series of PBM-CFD simulations in commercial code considering a two-way coupled liquid–solid multicomponent flow and a kinetic formulation similar to that of the F–W two-step mechanism. The reactive system included a simplified reduction reaction, $AgNO_3 + e \rightarrow Ag_{(l)}$, that leads up to nucleation and growth. In their PBM-CFD simulations, however, the authors neglected the contribution of particle diffusion and agglomeration on the PSD, which does not allow for a complete characterisation of the links between hydrodynamics and kinetics, and how these influence particle size.

From the preceding literature review it is clear that, while much progress has been made in the area of NP synthesis and its mechanistic modelling, multiple aspects remain elusive. Notably, a unifying scheme is needed to bridge the realm of the well-mixed systems considered in models akin to the F–W two-step mechanism and that of the continuously interdependent hydrodynamic phenomena inherent to continuous-synthesis reactors, including microfluidic channels, where little has been explored in terms of modelling reduction-based NP production. Moreover, and as explicitly remarked in Perala and Kumar [33], the field would greatly benefit from additional assessments of the capabilities of the F–W mechanism in explaining the temporal evolution of the PSD in well-mixed reactors through the systematic testing of different types of NPs.

In this study we propose for the first time a comprehensive modelling framework for extending the F–W two-step mechanism to continuous flows in order to predict the PSD for the synthesis of AgNPs in microfluidic channels. Mixing, particles diffusion, agglomeration, and other non-negligible hydrodynamic phenomena are all intertwined in the PBM-CFD model and directly linked to the reaction kinetics of reduction, nucleation, and growth. Through this framework – which represents a modelling novelty given that our approach is based on a reduction-driven synthesis – and experimental measurements, we investigate the effect of several operating conditions on the predicted particle size and polydispersity. We implement the proposed PBM-CFD model in the well-established open-source platform OpenQBMM [43]. The model was validated by extensive set of experiments, which also provided kinetic constants for our simulations.

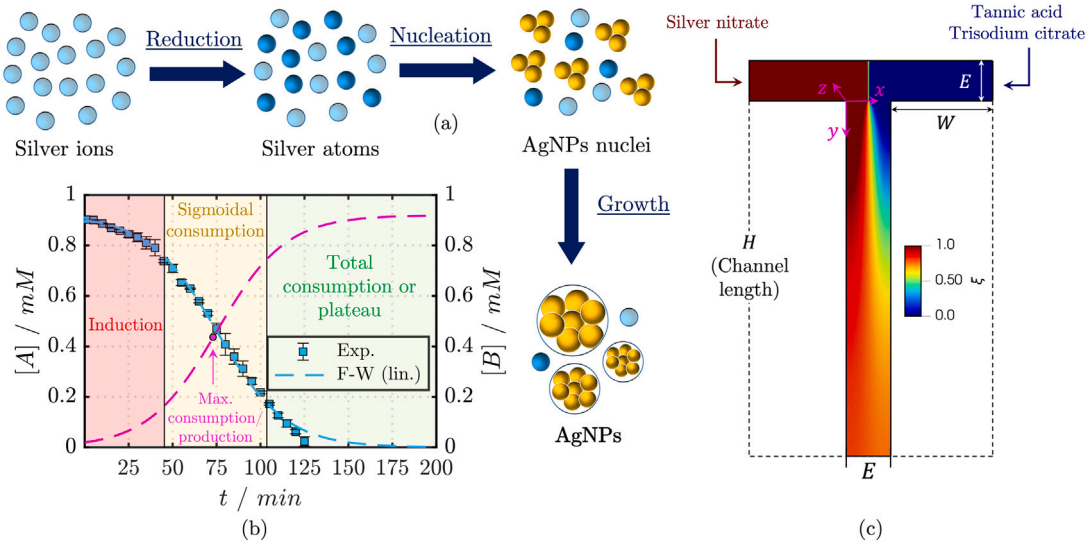

Fig. 1. Microfluidic synthesis of AgNPs via chemical reduction. (a) Simplified schematic of the reduction, nucleation, and growth steps, where the light blue spheres represent silver ions in solution, the dark blue spheres are the ions that have reduced into silver atoms, and the yellow spheres are NP nuclei that grow into AgNPs. (b) Example of temporal consumption and production of silver precursor (A, left axis, blue) and AgNPs (B, right axis, magenta), respectively, in a well-mixed reactor. The marks correspond to experimental measurements, as detailed in Nathanael et al. [44] and Section 2, and the dashed lines to their predicted values employing the F–W two-step mechanism in its linear form (see Eq. (5)). The operating conditions and kinetic constants correspond to those ascribed to the baseline case (see Section 2.3). (c) (not to scale) Schematic of the T-junction microchannel considered with a contour plot of the mixture fraction, $\xi = \frac{[SN]-[R]+[R]_0}{[SN]_0+[R]_0}$ (see Eq. (21)). The location of the Cartesian axis represents the outset of the geometrical domain $(x = 0, y = 0, z = 0)$.

2. Problem formulation and experimental methods

2.1. Operating conditions in a T-junction microfluidic device

The chemical synthesis process under consideration involves the reduction of silver nitrate, $AgNO_3$ (SN), in the presence of tannic acid, $C_7H_{52}O_{46}$ (TA), and trisodium citrate, $Na_3C_6H_5O_7 \cdot 2H_2O$ (TC) in a T-junction microfluidic device (see schematic in Fig. 1(c)). The inlet concentration of the reagents corresponds to 0.92 mM, 0.123 mM, and 1.91−3.82 mM for SN, TA, and TC, respectively; all reagents used were purchased from Alfa Aesar. Taking into account that each molecule of TA can reduce up to 20 silver ions [45] and each molecule of TC can reduce 4 silver ions [46], the concentrations of both TA and TC are set in excess. For example, the molar ratio of TA to SN is 0.05 based on the stoichiometry but in the investigated case is 0.13. The pH of the TA/TC inlet solution is adjusted to 7 and 12 using 0.1 M NaOH. This chemical method for the production of AgNPs is based on the protocol developed and tested in Kašpar et al. [47].

The continuous-flow setup was arranged by employing a Tee tubing junction (0.020″ Thru-Hole) (Upchurch Scientific), a syringe pump (World precision instrument-AL-4000) equipped by two 5 mL syringes (Fisher), two polytetrafluoroethylene (PTFE) tubes as inlet channels (ID = 500 μm, E in Fig. 1(c)) to provide the solutions of SN and the mixture of TA/TC, respectively, and an outlet PTFE tube (ID = 500 μm and total length = 2 m, E and H in Fig. 1(c), respectively) as a reaction outlet channel.

2.2. Measurements of silver ions concentration and PSD along the channel in the T-junction device

The concentration of silver ions is measured using a silver electrode (EDT direction) connected to a mV meter (Mettler Toledo-FP20) calibrated by standard solutions. A series of standard solutions (0.1,1,5,10, 100 ppm) are prepared by the dilution of the stock solution, which corresponds to a silver standard solution 1000 ppm, purchased from EDT direction. For high-level measurements above 50 ppm, 1 mL of 5 M ionic strength adjustment buffer (ISAB) is added. A calibration curve was prepared using the mV values on a linear axis and the concentration of silver ions on the log scale.

The synthesis of AgNPs is performed as described in the previous subsection under varying conditions of inlet flow rates ($Q = 200, 100, 67$, and 50 μL/min) and channel outlet lengths (0.1, 0.5, and 1 m). The samples are collected in triplicate after ∼ 240 s of operation for each of the outlet tube lengths. We note that our experimental setup does not allow for real-time *in situ* measurements of the concentration of silver ions in the microchannel. Therefore, whilst the collection of the sample is made at 240 s, the actual measurement is conducted after a certain period that corresponds to the transportation time of the sample. The calibration curve is used to determine the unknown sample concentrations. We make the note that in our operation the flow rate is set to be equal in both inlet channels. Hence, Q denotes the flow rate of each individual inlet ($Q_{total} = 2 \times Q$).

The PSD of the synthesised AgNPs is measured in triplicate using a Zetasizer Nano series (Malvern) with a refractive index of AgNPs set equal to 0.135 [48]. We highlight that zetasizer equipment provides measurements of PSD based on the assumption that the particles are spherical. For the interested reader, figure S4 of SI presents a comparison between PSDs measured using dynamic light scattering with the Zetasizer and a transmission electron microscope. The close agreement between measurements using these two techniques supports the approximation of spherical particles. Furthermore, it is relevant to remark that our synthesis protocol, employing TA and TC, has been utilised in previous studies, such as the work of Ranoszek-Soliwoda et al. [49], which also reported the synthesis of spherical particles under similar conditions. The PSD measurements are carried out under similar synthesis conditions as the above-explained measurements of silver ions concentrations ($Q = 200, 100$, and 50 μL/min at 0.25, 0.5, 1, and 2 m along the channel). The samples are collected in ice to quench further reactions.

2.3. Determination of the nucleation and growth constants according to the F-W two-step mechanism

The nucleation, k_1, and growth, k_2, rate constants describing the synthesis of AgNPs under different conditions of pH and $[TC]_0$ were taken from our previous work [44]. Please refer to its contents for an in-depth description of the methodology followed; here, we summarise

the most important details. The kinetic constants are determined from the absorbance intensity at 400 nm (characteristic of AgNPs) based on the F–W two-step mechanism. The time dependence of their absorbance is measured by UV–Vis spectrophotometer (Jenway-6300) and recorded every 5 min. The chemical reactions are carried out in a beaker and mixing is set at a point where the AgNPs synthesis reaction was independent of mass transfer (rotation velocity equal to 3000 rpm). The PSD of the synthesised AgNPs in a beaker is also measured in triplicate from three independent experiments by Zetasizer Nano series (Malvern). The values of k_1 and k_2 are estimated for the different conditions using the integrated form of the F–W mechanism, as expressed in Eq. (5). For curve fitting procedures, the value of $[A]$ is estimated using Eq. (11), as shown below [50]:

$$\left([A_o]-[A]\right)/[A]=\alpha/(1-\alpha). \tag{11}$$

In Eq. (11), α is $A/[A_\infty]$ and A and A_∞ are the maximum absorbance at time t and at long times, respectively. By plotting $\ln(a/1-a)$ versus t, a straight line with a slope and intercept is obtained, see figure 4(c, d) in Nathanael et al. [44], providing values for k_1 and k_2.

For an easier discussion of the results, we define a 'baseline' set of operating parameters and conditions as follows: $Q = 200$ μL/min, $pH = 7$, $[SN]_{0,inlet} = 0.92$ mM, $[TA]_{0,inlet} = 0.123$ mM, and $[TC]_{0,inlet} = 1.91$ mM, where, for example, $[SN]_{0,inlet} = 0.92$ mM corresponds to the initial or inlet concentration of SN in the well-mixed reactor or in the T-junction microchannel, respectively. Unless stated otherwise, the experimental and simulation results are reported under these 'base' conditions, from which different operating conditions are varied systematically.

3. Numerical methods and model description

This section introduces all relevant details of our proposed PBM-CFD numerical framework. We begin by providing a description of the simplified formulation for systems consistent with the original assumptions of the F–W two-step mechanism (i.e., well-mixed batch reactors) and present a validation of our implementation in open-source software. We then explore the intricacies of expanding the model to account for the dynamics of continuous-flow and non-premixed systems and outline the proposed modifications to the well-mixed reactor model .

3.1. Well-mixed reactor model formulation and initial code validation

In the PBM adopted in this work the PSD is described in terms of a univariate number density function (NDF), $f(L,t)$, with particle size L as internal coordinate. The NDF is defined in such a way that the quantity $f(L,t)\mathrm{d}L$ corresponds to the number density of particles with size in the interval L and $L+\mathrm{d}L$ at time t. Considering this definition, we henceforth refer to the NDF as the PSD of our particle sample or use both terms interchangeably. The governing population balance equation (PBE) is solved via the quadrature method of moments (QMOM) [1] in terms of the kth-order moment of the distribution, $m_k(t) = \int_0^\infty f(L,t)L^k\mathrm{d}L$, as depicted in the transport equation of Eq. (12); we refer the reader to Marchisio et al. [1] and Passalacqua et al. [43] for the full derivation of this equation from the moment transformation of the PBE, its subsequent closure via QMOM and the NDF reconstruction, and to Yuan [51] for a review of some of the existing quadrature-based moments method (QBMM). Here, we present a summary of the most noteworthy aspects. In line with the QMOM [52], the NDF is approximated by a finite summation of Dirac delta functions as follows: $f(L,t) \approx \sum_{i=1}^{N} w_i(t)\delta(L-L_i(t))$, so that $m_k(t) \approx \sum_{i=1}^{N} w_i(t)L_i^k(t)$, where L_i and w_i are respectively the abscissas and weights of the ith node of the quadrature, $\delta(L-L_i(t))$ is the Dirac delta function and N corresponds to the number of nodes of the quadrature approximation. In this approximation, the first $2N$ moments of the PSD are transported, namely $\{m_k\}$ with $k=[0,\ 2N-1]$. The weights and the abscissas of the quadrature approximation are calculated by the inverting the moments set, $\{m_k\}$, using the Wheeler algorithm [53].

The advantage of using QBMM is twofold: first, it solves a limited number of scalar transport equations for each moment, lowering the corresponding computational cost compared to class- [54] and Monte-Carlo-based methods [55]; second, the moments set represents physical measurable quantities of interest, making QBMM readily compatible with macroscopic modelling through CFD [1]. For instance, m_0 corresponds to the NPs number density, m_3 is proportional to the NPs volume fraction $\phi_d = k_V m_3$, where k_V is a volumetric shape factor, and the ratio m_{k+1}/m_k represents the mean particle size. The PBE for the well-mixed reactor is shown in Eq. (12):

$$\frac{\partial m_k(t)}{\partial t} = k\sum_{i=1}^{N} L_i^{k-1}G(L_i,y_j)w_i + J(y_j)d_{crit}^k, \tag{12}$$

where, from left to right, the terms represent accumulation, growth, and nucleation, respectively; $G(L_i,y_j) = dL_i(y_j)/dt$ is the growth rate, $J(y_j)$ is the nucleation rate, d_{crit} is the homogeneous NP nuclei size, and y_j represents the mass fraction of the species j in mixture. The expressions that define $G(L_i,y_j)$ and $J(y_j)$ are taken from the framework introduced in Perala and Kumar [33]:

$$J(y_j) = N_{av}\left(\frac{d_m}{d_{crit}}\right)k_1C_A(y_j), \tag{13}$$

$$G(y_j,L) = \frac{1}{3}k_2LC_A(y_j), \tag{14}$$

where N_{av} is the Avogadro number and d_m is the atomic diameter of silver so that d_{crit}/d_m corresponds to the number of silver atoms in a nucleus [33]. From Eqs. (13)–(14), it can be noticed that the growth and nucleation rates depend on the molar concentration of A, C_A, which itself depends on y_j (the mass fraction of species j in the mixture). For simplicity, we henceforth use the symbols $[j]$ and C_j interchangeably to denote the molar concentration of species j ($C_j = \rho_c y_j/MW_j$, wherein ρ_c is the density of the continuous phase and MW_j the molecular weight of j). The molar concentration of species j is obtained here from the F–W expressions for A and B (Eq. (3)), written in our framework as $\mathrm{d}(\rho y_j)/\mathrm{d}t = MW_jS_j$, where S_j is the mass-based source term representing the chemical reactions of nucleation and growth. Here, we have transformed the expression shown in Eq. (12) of Perala and Kumar [33] from a volume-based to a length-based NDF assuming spherical particles: $G(L,y_j) = (3/\pi)G(V,y_j)/L^2$, where $G(V,y_j)$ is a volume-based growth rate. This expression assumes that particle growth in length (diameter) is proportional to particle size. This is consistent with the aforementioned F–W assumption, in which all atoms in a NP contribute to particle growth, not just those located at the surface.

Takesue et al. [56] pursued an experimental investigation to explore the synthesis of AgNPs in the presence of TA and TC at pH = 12 and provided evidence to suggest that the process of AgNP nucleation is dominant during the first ~ 0.59–0.98 ms of operation, in which nuclei of size ~ 0.7 nm (Ag_{13} atom clusters) are predominately formed. Nevertheless, their small-angle X-ray scattering (SAXS) measurements also revealed the existence of clusters of Ag atoms of size ~ 1.2 nm (Ag_{55}). To the best of the authors' knowledge, Takesue et al. [56] remains one of the few available studies that tackle the problem of estimating d_{crit} under reactive conditions similar to those examined in the present investigation. Considering this, we use d_{crit} as one of the fitting parameters of our PBM-CFD model in the range $0.7 < d_{crit} < 1.35$ nm and report the value that better matched the experimental measurements in each case. This practice of tuning the PBM results using d_{crit} has previously been adopted by Perala and Kumar [33].

The mathematical framework described in this work is implemented in the C++ suite of PBM solvers *OpenQBMM* [43,57], which itself is built upon the finite volume method package *OpenFOAM*. To this end, a new solver based on the already existing application, *pbeFoam*, was

created to add the nucleation and growth models, as well as transport equations for each chemical compound in the system. For further details regarding the moment inversion algorithm, the discretisation schemes, the computation of the spatial fluxes (see next sub-section), and the general code structure, please refer to Passalacqua et al. [43].

We validate our code implementation by replicating the numerical results reported in Perala and Kumar [33] (see figure 2 of this reference) and the experimental measurements of Watzky et al. [2] employing our own PBM-CFD framework in the context of IrNPs synthesis and the original F–W two-step mechanism. Fig. 2(a)–(c) show the temporal evolution of the average particle diameter, d, the standard deviation, σ, the molar concentration of a reporter species C (proportional to the Ir precursor), and the zeroth-order moment, m_0. The chemical compound C – a particularity of the synthesis process of IrNPs – is consumed 1400 times faster than A in the growth reaction and has an initial concentration 1375 times higher than that of A; a transport equation analogous to $\mathrm{d}(\rho y_j)/\mathrm{d}t = MW_j S_j$ was added for C. The approximated PSD is reconstructed in line with the QMOM approach introduced above from a moments set $\{m_k\}$ with a number of quadrature nodes $N = 3$ and assuming a normal distribution. $N = 3$ represents a reasonable trade-off between computational cost and accuracy of the reconstructed NDF. This reconstruction was achieved following the technique described by John et al. [58].

For the case reported in Fig. 2, we have transformed our reconstructed distributions to be directly comparable with the results of Perala and Kumar [33], retrieved from a volume-based PBM. Considering the length-to-volume moment transformation $m_{k,V}(t) = k_V^k m_{3k,L}(t)$ for spherical particles [1] (the subscripts V and L represent volume- and length-based, respectively), the expression for average particle size of Perala and Kumar [33] in volume space (Eq. (15), $k_V = \pi/6$) becomes Eq. (16) in length space:

$$d_V(t) = \left(\frac{1}{k_V}\frac{m_{1,V}(t)}{m_{0,V}(t)}\right)^{1/3}, \tag{15}$$

$$d_L(t) = \left(\frac{m_{3,L}(t)}{m_{0,L}(t)}\right)^{1/3}. \tag{16}$$

We note that this definition of d is only used for comparison against Perala and Kumar [33]; for comparison against our experiments, we use $d = m_{k+1}/m_k$, as explained previously. The virtually superposed curves of Fig. 2 suggest a correct implementation and solution of the model within our PBM-CFD framework for the operating conditions and closing parameters (k_1, k_2, d_{crit} and d_m) considered in Perala and Kumar [33]. The excellent predictions against the experiments of Watzky et al. [2] and their derived expression (Eq. (6)) for d, in conjunction with the considerable discrepancies revealed when looking at σ, are a reflection of the potential shortcomings of the original F–W two-step mechanism in fully explaining the behaviour of the PSD, as detailed in the literature review of Section 1. Nonetheless, we make the brief note that part of the deviation in σ found in Perala and Kumar [33] is likely related to the choice of representing the mean diameter by lower-order moments (refer to §1 of SI for further details). We also highlight from Fig. 2(b) that, barring the outlier point at $t \approx 1.71$ h, the experimental data of σ appear to adopt an essentially constant behaviour at $t > t_{ind}$, while both d and m_0 continue to rise well after t_{ind}. As seen in the temporal reconstructions of the PSD of Fig. 2(d), the breadth of the distribution sharply rises after t_{ind} and continues to do so until the precursor has been fully consumed (see distributions at $t = 2$–27 h). The low size polydispersity of the experiments is explained by either a continuous nucleation process (as seen in the m_0 plot of Fig. 2(c)) where the nucleated particles are allowed to grow at a faster rate than larger particles to increase (decrease) the average size (standard deviation), as stated in Handwerk et al. [31], or the nucleation process promptly finishes after t_{ind}, as argued by Perala and Kumar [33]. This will be further discussed in Section 4.1 for the synthesis process under examination in this paper (AgNPs).

3.2. Model extension in a T-junction channel and simulation setup

The well-mixed reactor model based on the F–W two-step mechanism previously introduced is expanded to reach the domains of continuous-flow systems by first ascribing the conditions of low particle Stokes number, $St_d \ll 1$, and largely diluted solid–liquid flow (particle volume fraction, $\phi_d \ll 1$) to the system at hand, in alignment with the approach followed in Schikarski et al. [40] for a similar system. $St_d = t_d/t_{res}$, where $t_d = \rho_d L^2/18\mu_c$ and t_{res}, defined in Section 4.2.1, refer to the characteristic relaxation time of the particles and the residence time of the flow, respectively [1]. From experimental measurements of particle size, we have estimated that $St_d \sim O(10^{-10})$ - $O(10^{-7})$ for the system under investigation. Consequently, we adopt a one-phase formulation in which the particles (disperse phase, denoted by d) follow the fluid flow inertia (continuous phase, c).

The flow of the continuous phase, assumed to be incompressible and Newtonian, is governed by the continuity and momentum equations:

$$\begin{aligned} \nabla_{\mathbf{x}} \cdot \mathbf{u} &= 0, \\ \rho\left(\frac{\partial \mathbf{u}}{\partial t} + \mathbf{u}\cdot\nabla_{\mathbf{x}}\mathbf{u}\right) &= -\nabla_{\mathbf{x}} p + \nabla_{\mathbf{x}}\cdot\left[\mu(\nabla_{\mathbf{x}}\mathbf{u} + \nabla_{\mathbf{x}}\mathbf{u}^T)\right], \end{aligned} \tag{17}$$

where $\mathbf{u}$ corresponds to the fluid velocity, p is the pressure, ρ and μ are the fluid density and viscosity, respectively, under diluted conditions. A reduction reaction occurring prior to nucleation is added to account for the influence of mixing between the precursor and the reducing agent in the microreactor, in line with previous works [42,59]. The set of chemical reactions considered for our system and their respective reaction rates read:

$$\begin{aligned} &Reduction: SN + \nu_R R \xrightarrow{k_r} Ag_{(l)}; \\ &\qquad \dot{r}_r = k_r[SN][R]^{\nu_R}, \end{aligned} \tag{18}$$

$$Nucleation: Ag_{(l)} \xrightarrow{k_1} Ag_{(s)}; \quad \dot{r}_1 = k_1[Ag_{(l)}], \tag{19}$$

$$\begin{aligned} &Growth: Ag_{(l)} + Ag_{(s)} \xrightarrow{k_2} Ag_{(s2)}; \quad \dot{r}_2 = k_2[Ag_{(l)}][Ag_{(s)}] \\ &\qquad Ag_{(l)} + Ag_{(s2)} \xrightarrow{k_2} 2Ag_{(s2)}; \quad \dot{r}_{2'} = k_2[Ag_{(l)}][Ag_{(s2)}], \end{aligned} \tag{20}$$

where R corresponds to the reducing agent, $Ag_{(l)}$ to reduced silver atoms, $Ag_{(s)}$ to nuclei of nanoparticles, and $Ag_{(s2)}$ to those nuclei that have grown into AgNPs; ν is the stoichiometric coefficient of the species involved in the reduction reaction and the different k parameters correspond to the reaction rate constants. To avoid confusion, we make the note that in the continuous-flow model, we refer to the silver precursor (silver nitrate) by SN, whereas in the well-mixed reactor model, we use the symbol 'A' (see previous sub-section). We make this distinction given that the addition of the reduction reaction strongly alters the precursor's temporal consumption and influence over how nucleation and growth evolve, as discussed in the results section.

The mass fraction field of each chemical species in the microreactor is given by Eq. (21). This expression represents the conservation of the partial mass of species j, which incorporates Fick's law of diffusion and includes a source term that models species' mass exchange due to the chemical reactions. This source term is given by the elementary reactive source term of Eqs. (22)–(23):

$$\frac{\partial(\rho y_j)}{\partial t} + \nabla_{\mathbf{x}}\cdot(\rho \mathbf{u} y_j) = \nabla_{\mathbf{x}}\cdot(D_j \nabla_{\mathbf{x}}(\rho y_j)) + S_j, \tag{21}$$

$$S_j = MW_j \sum_{rxn=1}^{N_{rxn}} \hat{S}_{j,rxn} \tag{22}$$

$$\hat{S}_{j,rxn} = (\nu''_{j,rxn} - \nu'_{j,rxn})\left(k_{rxn}\prod_{j=1}^{N} C_{j,rxn}^{\nu''_{j,rxn}+\nu'_{j,rxn}}\right), \tag{23}$$

where D_j is the mass diffusion coefficient of species $j = (SN, R, Ag_{(l)}, Ag_{(s)}, Ag_{(s2)})$, rxn is an index denoting a specific reaction, N_{rxn} is the total number of reactions that involve species j; $\nu''_{j,rxn}$ and $\nu'_{j,rxn}$ are the stoichiometric coefficients of species j as it is produced and consumed

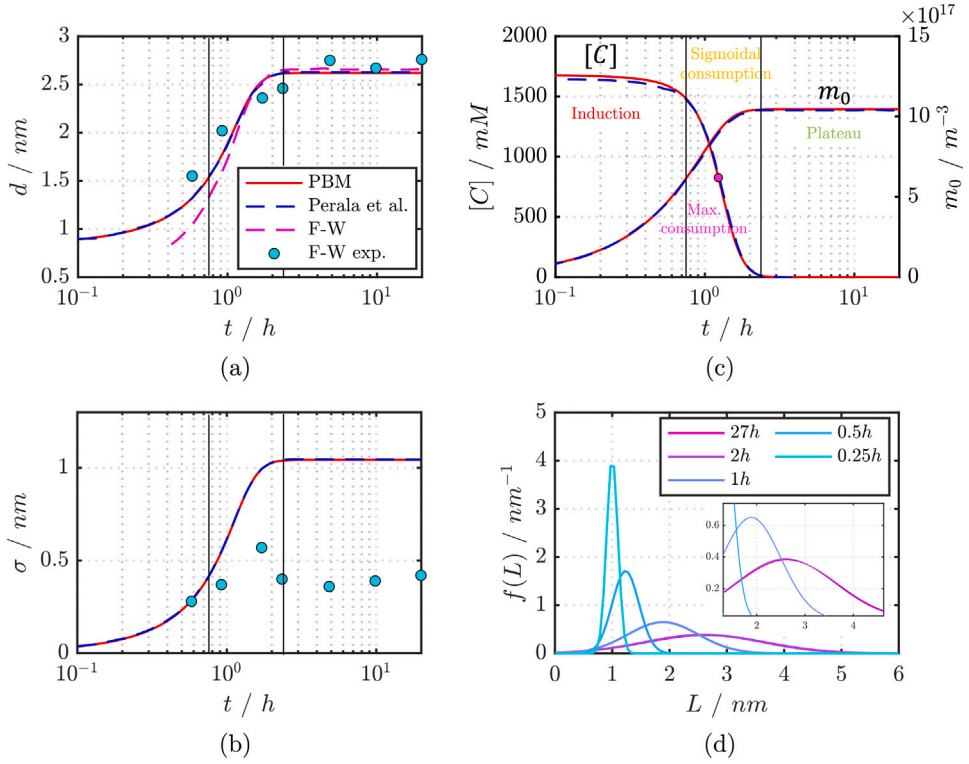

Fig. 2. Code validation against the numerical results of Perala and Kumar [33] and the experimental data of Watzky et al. [2] for IrNPs. Temporal evolution of (a) Average particle diameter and (b) standard deviation. The marks correspond to the experimental measurements of Watzky et al. [2] and the discontinuous magenta-coloured dashed line to the model proposed in the same reference (see Eq. (6)). (c) Molar concentration of reporter species and zeroth-order moment and (d) Evolution of normal PSD in time. The continuous vertical lines separate the stages of induction, sigmoidal consumption, and plateau. $[A]_0$ = 1.2 mM, $[B]_0$ = 0.0 mM, $[C]_0$ = 1650 mM, k_1 = 0.0282 h^{-1}, k_2 = 3.379 × 10^3 $M^{-1}h^{-1}$ ($[A]_0k_2/k_1$ = 159.52), d_{crit} = 0.83 nm, d_m = 0.272 nm; $t_{ind,j}$ = 0.89 h, $t_{ind,p}$ = 0.75 h, t_{max} = 1.22 h.

in reaction *rxn*, respectively. The mass fraction of H_2O is obtained from the algebraic relationship: $y_{H_2O} = 1 - \sum_{j=1}^{N-1} y_j$.

Ranoszek-Soliwoda et al. [49] have documented the potential formation of a TA-TC complex from a solution containing these two chemical reagents, wherein the complex performs a double action as reducing and stabilising agent in the synthesis of AgNPs. These observations pose additional modelling challenges given the current uncertainty regarding the reducing strength of such complex, its transport and molecular properties, and the exact stoichiometry and kinetics of a simplified reduction reaction, such as Eq. (18), which are largely unexplored topics in the literature. Consequently, the framework of a generic reducing agent with transport and molecular properties equal to those of TA was adopted herein. This is because the molecular weight of this species significantly exceeds that of TC (MW_{TA} = 1.70 kg/mol and MW_{TC} = 0.29 kg/mol), thus, the transport of a potential TA-TC complex via diffusion will be greatly limited by the large-sized molecule of TA in comparison to TC ($D_{TA} \sim 2.17 \times 10^{-10}$ m^2/s and $D_{TC} \sim 1.74 \times 10^{-9}$ m^2/s [60]). In light of these uncertainties, and taking into account the comparatively much lower inlet concentration of TA with respect to TC (see Section 2.1), we have tested the effect of ν_R and k_r on the consumption of SN across the channel (see Fig. 6(b)–(f) in Section 4.2.1). By expanding the PBE to include the effects of convection in physical space, diffusion, and particle aggregation, Eq. (24) is obtained:

$$\frac{\partial m_k(t,\mathbf{x})}{\partial t} + \nabla_{\mathbf{x}} \cdot [\mathbf{u} m_k(t,\mathbf{x})] = k \sum_{i=1}^{N} w_i L_i^{k-1} G(L_i, y_j) + \nabla_{\mathbf{x}}^2 \cdot \sum_{i=1}^{N} \left[\frac{D_0 L_0 w_i L_i^k}{L_i + L_0} \right] + \mathcal{B}(L_i)^{agg} - \mathcal{D}(L_i)^{agg} + J(y_j) d_{crit}^k. \quad (24)$$

The expressions for nucleation and growth used correspond to those found in Eqs. (12)–(14) for the well-mixed reactor model. Nevertheless, here, J and $G(L)$ are functions of $C_{Ag_{(l)}}$ instead of C_A, making $C_{Ag_{(l)}}$ the driving force for nucleation and growth in the continuous-flow model; **u** is the particles' velocity (equal to the velocity of the continuous phase). The mass diffusion coefficient is computed using the size-dependent Stokes-Einstein (S-E) relation, $D_L = D_0/L$, where $D_0 = \frac{k_B T}{3\pi\mu_c}$ (k_B is the Boltzmann constant and T the temperature of the system). In this study, the average particle sizes in the microreactor range from d_{crit} to 22 nm (see e.g., Fig. 8), corresponding to mass diffusion coefficients in the range 7.0×10^{-10} - 2.2×10^{-11} m^2/s. These values are entirely comparable to the experimental measurements of Ung et al. [61], which place the mass diffusion coefficient of AgNPs in an aqueous solution at $\approx 5.38 \times 10^{-11}$ - 2.56×10^{-11} m^2/s for particle sizes in the range 9.84–18.5 nm. The validity of the S-E expression is contingent upon its assumptions, which include fully spherical particles, low particle volume fractions, and negligible particle interactions [1,62]. As discussed in Section 2.2, our experimental measurements of PSD using two different techniques (see figure S4 of SI) suggest that the synthesised particles are spherical under our operating conditions. These measurements, combined with the highly diluted conditions of our system ($\phi_d \ll 1$, discussed previously) and the accurate predictions against experimental data, provide evidence supporting the validity of the S-E equation, which has also been used to estimate the mass diffusivity of similar NPs in previous investigations [39].

All terms on the RHS of Eq. (24) have been closed via the QMOM introduced above. It is noteworthy to point out the closure related to the diffusion term in physical space. This closure involves the introduction of a small non-zero term, $L_0 \sim O(10^{-12})$ m, to make $f(L)$ non-zero in the domain of the internal variable $[0, \infty)$ [1]. $\mathcal{B}(L_i)^{agg}$ and $\mathcal{D}(L_i)^{agg}$ are the birth and death rate of particle size L_i due to agglomeration;

with the QMOM closure they read as follows [1]:

$$\mathcal{B}(L_i)^{agg} - \mathcal{D}(L_i)^{agg} = \frac{1}{2}\sum_{i}^{N}\sum_{l}^{N} w_i w_l \beta_{Br}(L_i, L_l)\left[(L_i^3 + L_l^3)^{k/3} - L_i^k - L_l^k\right], \tag{25}$$

where $\beta_{Br}(L_i, L_l)$ is the Brownian aggregation kernel stating the rate at which two particles of sizes L_i and L_l collide and aggregate due to Brownian diffusive phenomena:

$$\beta_{Br}(L_i, L_l) = \frac{2k_B T}{3\mu}\frac{(L_i + L_l)^2}{L_i L_l}. \tag{26}$$

This collision kernel was selected to model aggregation, in line with the laminar nature of the system, the small particle sizes involved ($\ll 1$ μm) [1], and the comparatively large residence times involved in the microreactor, which allow for particle aggregation despite the presence of a stabiliser. Similar to the well-mixed reactor model, we implement the nucleation and growth models in conjunction with the species transport equations and the closure of the particle diffusion model making use of *OpenQBMM* and the baseline solver *buoyantPbePimpleFoam*. The simulation domain consists of a two-dimensional representation of the experimental T-junction channel (Fig. 1(c)) with two inlet streams of length $W = 10E$ and one outlet. Although the lengths of the inlet streams are shorter than their experimental counterparts, the simulated lengths suffice to obtain a fully developed inlet flow before mixing.

The boundary and initial conditions are as follows. A uniform velocity field is imposed at both inlets with a zero-gradient Neumann condition for pressure ($dp/d\mathbf{n} = 0$). At the outlet, the velocity is treated with a zero-gradient boundary condition whilst the pressure is appointed a fixed reference value. All moments are initialised in zero at the channel's domain with a zero-value Dirichlet boundary condition at the inlets and a Neumann condition at the outlet; the walls are treated as no-slip boundaries for all variables except for pressure, for which a zero-gradient boundary is employed. The temperature is kept constant at 298.15 K.

The governing equations are discretised in a finite-volume framework within a co-located mesh arrangement. The temporal terms are discretised through a first-order implicit Euler scheme, while all the divergence operators follow a first-order upwind Gaussian scheme and the Laplacian operators a second-order central-difference scheme. The pressure-velocity coupling follows the PISO (Pressure-Implicit-of-Split-Operations [63]) transient algorithm with a total of two correctors. We employ a semi-uniform Cartesian mesh of cell size $\Delta\mathbf{x} = (\Delta x, \Delta y, \Delta z) = (E/50, E/40, E)$ wherein the variables are solved in the $x - y$ 2-D plane with a global resolution of $\sim O(10^6)$ cells (see Section 2 of SI for a description of the mesh independence study performed). The time-step for the simulations was set to be adaptive according to the Courant–Friedrichs–Lewy (CFL) condition: $Co = \mathbf{u}\Delta t/\Delta\mathbf{x}_{min} < 1.0$. The simulations are run until all variables have reached a steady-state, which in most cases is attained at approximately $t = 20t_{res}$ (see Section 4.2.1 for the definition of t_{res}).

It is well-known [64,65] that first-order schemes introduce numerical diffusion to the solution through the leading term of the truncation error, which takes the form of a Laplacian term (e.g., $D_{num}\frac{\partial^2 y_j}{\partial x^2}$). For a first-order scheme applied to the temporal and convective terms, the numerical diffusion coefficient – denoted as D_{num} – which modulates the importance of this fictitious diffusion, can be estimated to be proportional to $\Delta\mathbf{x}$. As a consequence of the small mass diffusion coefficients involved in our system ($O(10^{-11})$ - $O(10^{-9})$ m^2/s for the inlet streams and AgNPs in liquid), we expect the error introduced by numerical diffusion to be most pronounced in regions characterised by significant spatiotemporal y_j and m_k gradients. As analysed throughout the manuscript, these primarily include the regions in the vicinity of the walls and the channel centre-line in the x-direction, where the inlet reagents streams first converge and react (see Fig. 7).

Further implications of employing a first-order upwind scheme, and how an increase in the mesh resolution attenuates the above-mentioned problems are discussed with the mesh independence test results (§2 of SI). Despite their proneness to numerical diffusion, first-order schemes offer the advantages of providing bounded solutions and ensuring numerical stability. These features hold significant value for our application given that we have variables with very specific limits ($0 < y_j < 1$) as well as variables whose range can vary several orders of magnitude (such as m_0). It is worth highlighting that, despite the small mass diffusivity coefficients involved, first-order upwind discretisation schemes for the convective term are common practice in the field of modelling the synthesis process of NPs [40–42].

To enhance the readability of the forthcoming discussions, we reiterate the extensions made to the F–W-based model for simulating synthesis in microfluidics. These extensions encompass the incorporation of a reduction reaction prior to nucleation and growth (Eq. (18)), adding reactive convection–diffusion equations for each species in the system (Eqs. (21)–(23)), including the space-dependent phenomena of convection and diffusion in the PBE (Eq. (25)), and adding an aggregation term.

4. Results and discussion

4.1. Effect of pH and $[TC]_0$ on the synthesis of AgNPs in a well-mixed reactor

In this subsection, we present an examination of the original F–W two-step mechanism in the context of AgNPs synthesis in a well-mixed reactor under different operating conditions. Fig. 3(a)–(b) depict the temporal consumption (production) of A (B) obtained by varying $[TC]_0$ experimentally (using the data from Nathanael et al. [44]) and via our well-mixed reactor model framework at $pH = 7$. The numerical results shown in these figures were obtained by solving the F–W-based mass conservation expressions for A and B ($\mathrm{d}(\rho y_j)/\mathrm{d}t = MW_j S_j$) in conjunction with Eqs. (12)–(14) to obtain the PSD, which is discussed later on in Fig. 4 and Table 2. Table 1 reports the values of k_1 and k_2 for each set of conditions, gathered from the F–W fittings described in Nathanael et al. [44], as well as the estimations of t_{ind}, t_{max}, and $t_{plateau}$ through Eqs. (7)–(10).

The kinetic curves of $pH = 7$ showcase the adoption of the typical behaviour outlined by the F–W two-step mechanism (induction, sigmoidal production/consumption, and plateau) and the excellent agreement with our simulations for the three $[TC]_0$ tested. The values of the ratio $k_2[A]_0/k_1 > 1$ of Table 1 suggest longer periods of nucleation ($t_{nuc} = 1/k_1$) compared to growth ($t_g = 1/k_2[A]_0$), at least initially, which limit the consumption of A during the induction period ($t < 40 - 60$ s).

A first look into the effect of $[TC]_0$ reveals an apparent non-monotonic response of A and B with $[TC]_0$, whereby the fastest consumption is seen for the lowest $[TC]_0$ (1.91 mM) and the slowest for the $[TC]_0$ immediately above (2.87 mM). This sort of non-monotonic response, which is also observed in t_{ind}, t_{max}, and $t_{plateau}$ (see Table 1), has been reported previously in the work of Sandoe et al. [66] for AgNPs synthesis in the presence of sodium citrate. The study above attributes this qualitative trend to the dual role of sodium citrate as a reducing (increasing k_1) or stabilising agent (decreasing k_1), depending on the concentration. The change in k_1 and k_2 seen in the present study by solely varying $[TC]_0$ and maintaining $[TA]_0$ constant suggests the incidence of coexisting stabilising and reducing effects of TC, as proposed in Ranoszek-Soliwoda et al. [49].

The experimental and well-mixed reactor PBM kinetic curves shown in Fig. 3(c)–(d) for $pH = 12$ display a distinctive behaviour that diverges substantially from that observed in $pH = 7$. On account of the one to two orders of magnitude higher k_1 at a similar k_2 for each $[TC]_0$ (see Table 1), the system undergoes an exceedingly fast induction period and exhibits a mode of behaviour more consistent with the

Table 1
F–W two-step mechanism fitting parameters according to the experimental measurements of Nathanael et al. [44] and summarised in Section 2.3 in a well-mixed reactor for the chemical synthesis of AgNPs. $[A]_0 = 0.92$ mM, $[TA]_0 = 0.123$ mM, $[B]_0 = 0$ mM.

pH	$[TC]_0$/mM	k_1/min^{-1}	k_2/M^{-1}min^{-1}	$k_2[A]_0/k_1$	$t_{ind,j}$/min	$t_{ind,p}$/min	t_{max}/min	$t_{plateau}$/min
7[a]	1.91[a]	0.0011[a]	55.51[a]	46.43[a]	48.32[a]	40.16[a]	73.57[a]	98.81[a]
7	2.87	0.0013	37.86	26.79	62.34	52.04	99.10	135.84
7	3.82	0.0015	44.81	27.48	46.73	39.37	77.56	108.38
12	1.91	0.1000	77.97	0.72	–	–	–	5.73
12	2.87	0.0120	13.66	1.05	–	0.63	1.88	55.48
12	3.82	0.0128	26.01	1.87	–	5.82	17.03	52.89

[a] Baseline case conditions, as defined in Section 2.3.

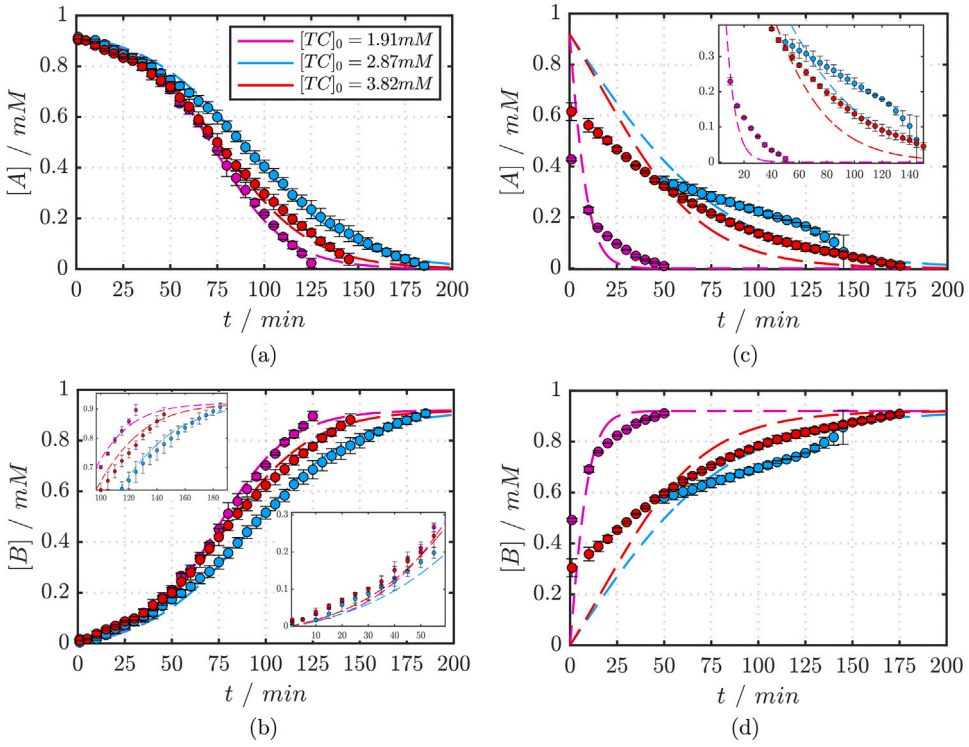

Fig. 3. Effect of pH and $[TC]_0$ on the temporal evolution of $[A]$ and $[B]$ and comparison between the experimental measurements of Nathanael et al. [44] (marks) and F–W-based PBM predictions (dashed lines) for AgNPs in a well-mixed reactor, showing how F–W predicts well the behaviour at $pH = 7$ but not at $pH = 12$. (a)–(b) $pH = 7$. (c)–(d) $pH = 12$. $[A]_0 = 0.92$ mM, $[TA]_0 = 0.123$ mM, $[B]_0 = 0$ mM. See Table 1 for k_1, k_2, and characterising times of induction and maximum rate of consumption/production.

decreasing and concave-up consumption of A that characterises the stages that follow the instance of maximum production of B (see $pH = 7$ curves at $t > 100$ min). In fact, the estimations of t_{ind} and t_{max} using the fittings of k_1 and k_2 lead to either negative (reported as '-' in Table 1) or significantly smaller values than their $pH = 7$ counterparts.

The almost immediate fast-rate consumption of A seen for the high pH cases is related to the high rates of nucleation that equalise the characteristic times of nucleation and growth ($k_2[A]_0/k_1 \sim 1$). The rapid kinetics governing the consumption of A under high pH conditions, as well as the virtual absence of an induction period found here, are in complete agreement with the experimental studies of Qin et al. [67] and Dong et al. [68], which have investigated the synthesis of AgNPs in the presence of ascorbic acid-sodium citrate and sodium citrate, respectively.

Opposite to $pH = 7$, the curves for $pH = 12$ exhibit noticeable disparities between the experimental measurements and the PBM results based on the F–W fittings for all three $[TC]_0$ tested . These discrepancies, which are especially apparent during the first ~ 50 min of operation, are an indication of the system not fully conforming to the assumptions of the original F–W two-step mechanism. As briefly alluded to previously, the quasi-equilibration of the characteristic times of nucleation and growth ($k_2[A]_0/k_1 \sim 1$, Table 1) indicate that a slow and continuous nucleation process does not ensue at $pH = 12$, as it is proposed in F–W. Instead, the large values of k_1 (approximately two orders of magnitude higher than in $pH = 7$), together with the aforementioned elimination of the induction period and the fast consumption of A, confirm the rapid emergence of NP nuclei within a small time span. As detailed in Nathanael et al. [44], the good F–W k_1 and k_2 fittings found for $pH = 12$ are only valid for ranges of the experimental data that exclude the measurements at early times ($t < 25$ min and $[A] > 0.6$). This fact further explains the increased deviations at those early reaction times and confirms that the assumptions of F–W are not applicable under alkaline conditions for our reaction system.

The PSD of the samples obtained after a total consumption of the precursor under the conditions of Fig. 3 is depicted in Fig. 4. Here, we plot the experimental measurements, a fitting of these to a normal distribution, and the PBM predictions. These predictions take the values of $d_{4,3} = m_4/m_3$ – the volume-weighted or De Brouckere mean diameter – as the basis for computing the average diameter, the coefficient of variation, and the standard deviation of the reconstructed normal distribution, in accordance with John et al. [58]'s technique. The practice of using high-order moments to represent the average size of a distribution has been widely adopted in solid–liquid and solid-gas modelling applications, including granulation and precipitation [69], given their direct relationship with the larger particles of the sample.

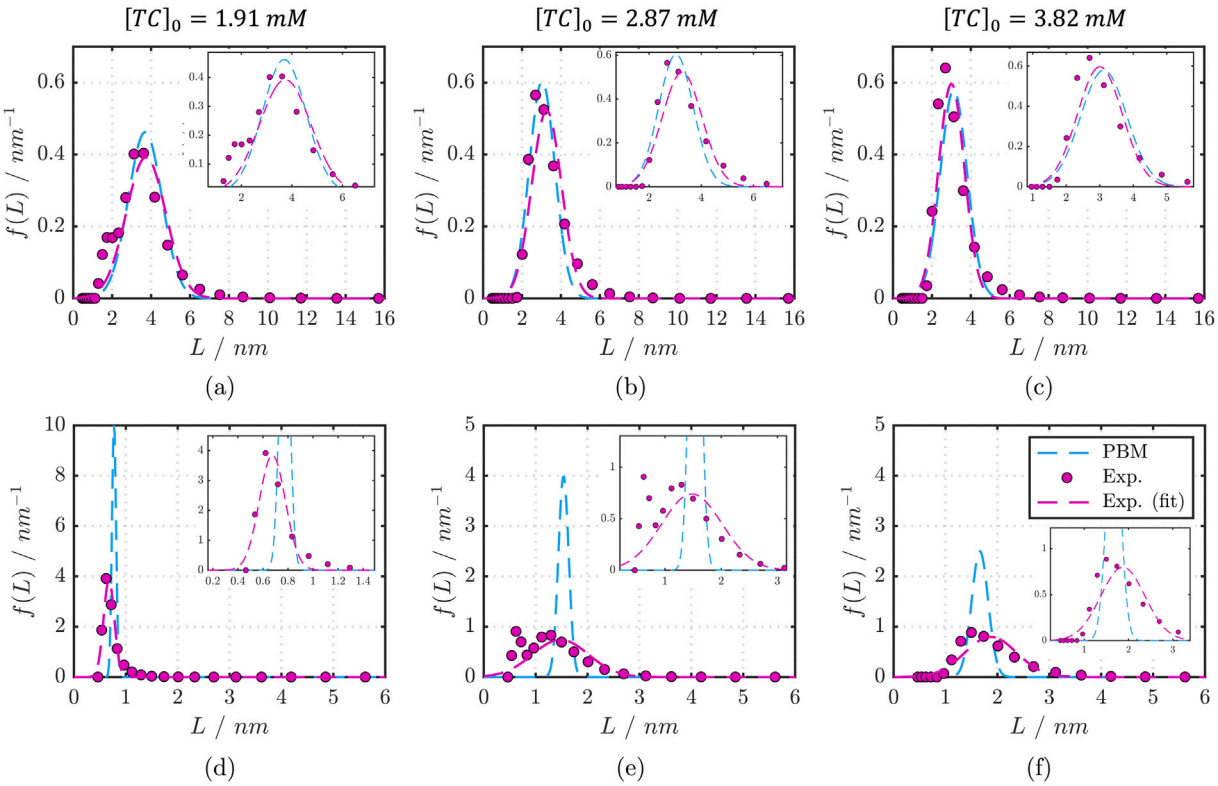

Fig. 4. Effect of pH and $[TC]_0$ on the PSD after full precursor consumption and comparison between experimental measurements, normal distribution fitting of said measurements, and F–W-based PBM predictions for AgNPs in a well-mixed reactor, highlighting the limitations of F–W for $pH = 12$. (a)–(c) $pH = 7$. (d)–(f) $pH = 12$. Left, middle and right panels correspond to $[TC]_0 = 1.91, 2.87, 3.82$ mM, respectively. $[A]_0 = 0.92$ mM, $[TA]_0 = 0.123$ mM, $[B]_0 = 0$ mM, $d_{crit} = 1.35$ nm, $d_m = 0.344$ nm. See Table 1 for k_1, k_2, and characterising times of induction and maximum rate of consumption/production.

The average particle size, standard deviation, and $PDI = (\sigma/d)^2$ of each case are compiled and summarised in Table 2. These results suggest an acceptable agreement between the experimental and F–W-based PBM distributions for $pH = 7$, with maximum deviations of 10.1% and 31.2% for d and σ, respectively (the maximum deviations against the fitted experimental data correspond to 7.2% and 13.6% for d and σ). As stated in Section 1, previous investigations have reported substantial discrepancies (up to 150%) against experimental measurements when attempting to employ the original F–W two-step mechanism to describe the behaviour of the PSD, notwithstanding the model's excellent predictive capabilities in terms of precursor consumption [33,36].

In alignment with Perala and Kumar [33], and as will become more apparent in our analysis of $pH = 12$, we observe an amplification of these discrepancies for σ when compared to d. We note, however, that our PBM simulations for all $pH = 7$ cases provide under-predictions of σ and the opposite is reported in Perala and Kumar [33] for IrNPs (see Fig. 2(b)). Our under-predictions of σ are likely caused by the choice of representing d by a volume-weighted average, which tends to be disproportionally influenced by the largest particles in the system, thereby resulting in slightly higher d and lower σ than would be obtained with lower-order moments, as calculated in Perala and Kumar [33] (see Eqs. (15)–(16)).

By examining the influence of $[TC]_0$ on the PSD at $pH = 7$, a similar non-monotonic behaviour mode as that seen in the consumption of A (Fig. 3) is detected for d and σ via the experiments and PBM simulations, with the exception of σ in the experimental data set, which exhibits a monotonically-decreasing trend with an increase in $[TC]_0$ (see Table 2). The adherence of the system to a non-monotonic response with the concentration of the stabiliser has been outlined previously in Das et al. [70] and Henglein and Giersig [71] . Nonetheless, we underline that a clear separation in the response of these variables can be noticed between $[TC]_0 = 1.91$ mM and the two higher concentrations, whereby the overall faster consumption of A appears to bring about higher d, σ, and PDI.

The comparatively small particle sizes induced by the two higher $[TC]_0$, together with our above-mentioned remarks in regard to the reaction kinetics and characterising times (see times in Table 1), are likely to be signs of the stabilising activities of TC under the conditions of reactants concentration and pH considered herein. Bastús et al. [72] have described similar findings, with a decrease in the initial TA/TC concentration ratio largely associated with the synthesis of smaller-sized AgNPs.

We continue our discussion by focusing on the results for $pH = 12$, where an evident performance deterioration of our F–W-based PBM predictions is identified, with the deviations of σ against the experimental measurements being particularly prominent (see Fig. 4(d)–(f)). Specifically, we find errors in the range 5.9 to 13.0% and 78.0 to 85.5% in terms of d and σ, respectively; as was the case for the lower pH cases, these σ deviations correspond to under-predictions for all three $[TC]_0$, as illustrated by the PBM peaks in $f(L)$. The source of these discrepancies in σ appears to be associated with the fast nucleation processes that govern the synthesis at alkaline conditions ($k_2[A]_0/k_1 \sim 1$) and that manifestly conflict with the assumptions of the F–W two-step mechanism of uncoupled nucleation and growth and that also disrupt the three well-defined stages of induction, sigmoidal growth, and plateau. Recalling our previous statements concerning the equilibration of the rates of nucleation and growth, the higher values of k_1 at $pH = 12$ allow for faster creation of nuclei of size d_{crit}, which in turn decreases the average diameter of the population, as captured by the model and observed experimentally. Nonetheless, as particle growth comes into play and halts significantly earlier at high pH (see t_{max} and $t_{plateau}$ in Table 1) due to the rapid depletion of A, the emergence of nuclei and their almost concurrent growth leads to a surge in size polydispersity that is not correctly explained by F–W.

Table 2
Effect of pH and $[TC]_0$ on d, σ, and $PDI = (\sigma/d)^2$ after full precursor consumption and comparison between experimental measurements, normal distribution fitting of said measurements, and F–W-based PBM predictions for AgNPs in a well-mixed reactor. $[A]_0 = 0.92$ mM, $[TA]_0 = 0.123$ mM, $[B]_0 = 0$ mM, $d_{crit} = 1.35$ nm, $d_m = 0.344$ nm.

pH	$[TC]_0$/mM	k_1/min^{-1}	k_2/M^{-1}min^{-1}	$k_2[A]_0/k_1$	$d \pm \sigma$/nm (PDI)		
					PBM	Exp.	Exp. (fit)
7[a]	1.91[a]	0.0011	55.51	46.43	3.60 ± 0.91 (0.064)	3.61 ± 1.30 (0.13)	3.74 ± 1.02 (0.07)
7	2.87	0.0013	37.86	26.79	3.03 ± 0.66 (0.048)	3.37 ± 0.96 (0.08)	3.26 ± 0.76 (0.05)
7	3.82	0.0015	44.81	27.48	3.12 ± 0.69 (0.049)	3.14 ± 0.94 (0.09)	3.00 ± 0.67 (0.05)
12[b]	1.91[b]	0.1000	77.97	0.72	0.77 ± 0.04 (0.003)	0.73 ± 0.18 (0.06)	0.68 ± 0.10 (0.02)
12	2.87	0.0120	13.66	1.05	1.54 ± 0.10 (0.004)	1.36 ± 0.57 (0.18)	1.48 ± 0.54 (0.13)
12	3.82	0.0128	26.01	1.87	1.66 ± 0.16 (0.009)	1.91 ± 1.10 (0.33)	1.87 ± 0.50 (0.07)

[a] Baseline case conditions, as defined in Section 2.3.
[b] For this case, $d_{crit} = 0.7$ nm.

The steep decline in d and σ with pH uncovered by the experimental and PBM results is in agreement with multiple instances in the literature for similar processes (see Nathanael et al. [27]). The work of Alqadi et al. [26], in addition to elucidating this inverse relationship, observed a more varied distribution in terms of particle shape at lower pH conditions. The authors postulated that this variability arises at low pH as a consequence of a mismatch in the rates of nucleation and growth, suggesting a strong connection with the F–W assumption of segregated nucleation and growth. Other authors [67,73] attribute the lower particle size at higher pH to a kinetic acceleration of the reduction reaction in particular, a statement consistent with the much marked rise in k_1 with pH than k_2 obtained here. Interestingly, the effect of $[TC]_0$ at $pH = 12$ appears to be opposite to that observed at a lower pH, with a higher concentration of TC resulting in larger-sized NPs, hinting at instances of TC promoting particle growth instead of obstructing its development and supporting the claims of 'double action' as stabiliser and reducing agent.

To finalise our discussion of the well-mixed reactor model results, we highlight the crucial importance of the ratio $k_2[A]_0/k_1 = t_{nuc}/t_g$ in predicting the PSD within the framework of the F–W two-step mechanism. The PBM results of Table 2 point to this ratio being a strong positive predictor of d, σ, and PDI; in fact, the results reported in Fig. 5 demonstrate that it is the sole predictor of these quantities after the plateau stage has concluded in the reactor. Fig. 5(a)–(f) illustrate the influence of this ratio by increasing k_1 and k_2 individually and conjointly one order of magnitude from the baseline conditions reported in Section 2. In the cases labelled as $k_2[A]_0/k_1$ and $10k_2[A]_0/10k_1$, after a steady-state is reached both show a virtually identical PSD and m_0, despite the latter case exhibiting a significantly faster NP production during the first stages due to its higher k_1 and k_2 (see $[B]$, m_0, and m_3). The balance attained in terms of particle size, standard deviation, and number of particles under the same $k_2[A]_0/k_1$ conditions is explained by noticing that the fast nucleation and growth processes that characterise $10k_2[A]_0/10k_1$ trigger a swift precursor consumption that quickly finalises at ~ 25 min of operation, whereby a large amount of nuclei form and grow in a limited time span. The slow processes of the case $k_2[A]_0/k_1$ allow the reactions to continue until ~ 175 min, providing the system with enough time to 'catch up' in size and number of particles to $10k_2[A]_0/10k_1$. As the quantity $k_2[A]_0/k_1$ increases (see case labelled $10k_2[A]_0/k_1$), the kinetic separation of nucleation and growth (comparatively slower nucleation) allows for the formation of enough nuclei to promote a fast NP growth step without completely consuming the precursor, leading to the large particle sizes observed for this case. In contrast, in the case labelled as $k_2[A]_0/10k_1$ the comparatively faster nucleation step brings about a large quantity of small-sized nuclei (see m_0) that do not grow at a sufficiently fast rate, which gives rise to a sample described by a low average particle size, akin to our experimental/simulation results at pH = 12. As expected, despite the highly varied temporal paths of NP formation for the four cases in Fig. 5(a)–(f), their equal $[A]_0$ produces very similar dispersion concentrations (see m_3, which is proportional to the volume fraction of the solid phase in liquid) after the full exhaustion of the precursor.

Additional numerical experiments were carried out to provide further evidence for these claims and to further untangle the relationship between $k_2[A]_0/k_1$ and PSD. In Fig. 5(g)–(i) we showcase the results of a five-orders-of-magnitude sweep of the ratio $k_2[A]_0/k_1$, made by varying its three constitutive parameters individually. Fig. 5 exhibits a clear collapse of all points into a single, monotonically increasing curve of d and σ vs. $k_2[A]_0/k_1$, which is fitted to a two-term power-law function and used to estimate the functional form of the PDI. We make the cautionary note that, as previously mentioned, the assumptions of the F–W two-step mechanism require comparatively slower nucleation processes ($k_2[A]_0/k_1 \gg 1$), which might render invalid the points collapse and power-law fitting for $k_2[A]_0/k_1 < 1$ (separated by the vertical dashed line in Fig. 5(g)–(i)). Our findings from the parameter sweep can be summarised as follows: in a well-mixed reactor, longer stages of nucleation in relation to growth give rise to a population of particles defined by higher (lower) d and σ (m_0). The aforementioned observations are broadly followed by the experimental data, as seen from Table 2, implying that a general tuning of the NPs size can be achieved by selecting the operating conditions that allow for a particular ratio between the initial characteristic times of nucleation and growth.

4.2. Synthesis of AgNPs in a T-junction microchannel

4.2.1. Precursor & consumption dynamics

As previously remarked, the transition from a spatially-averaged well-mixed reacting system to a continuous-flow environment uncovers multiple interacting phenomena that alter the synthesis process. Following previous approaches [37,39,40], we analyse a few relevant time scales and dimensionless numbers of the process in order to elucidate the governing mechanisms driving the synthesis of AgNPs. In our reduction-based PBM-CFD model, we consider the following events, each characterised by an individual time scale: (i) diffusive mixing of the reactant streams, t_{mix}, (ii) reduction reaction to produce silver atoms ($Ag_{(l)}$), t_r, (iii) nucleation, t_{nuc}, (iv) growth, t_g, (v) particle diffusion, t_{diff}, and (vi) particle agglomeration, t_{agg}. Taking into consideration that the driving force behind particle nucleation and growth is the concentration of $Ag_{(l)}$ (see Section 3.2), the stages of mixing and reduction that create the $Ag_{(l)}$ material and that themselves depend on the concentrations of the precursor and reducing agent (see Eqs. (18)–(20)), are particularly crucial to the process.

We define the following scaling, $\tilde{\mathbf{x}} = \frac{\mathbf{x}}{E}$, $\tilde{\mathbf{u}} = \frac{\mathbf{u}}{U_a}$, $\tilde{t} = \frac{t}{H/U_a}$, $\tilde{\rho} = \frac{\rho}{\rho_c}$, which renders Eq. (21) for the precursor and reducing agent dimensionless:

$$\begin{aligned}
&\frac{\partial(y_{SN})}{\partial\tilde{t}} + \frac{H}{E}\tilde{\nabla}_{\mathbf{x}}\cdot(\tilde{\mathbf{u}}y_{SN}) = \\
&\qquad \frac{1}{Pe_{SN}}\tilde{\nabla}_{\mathbf{x}}\cdot(\tilde{\nabla}_{\mathbf{x}}(y_{SN})) - Da_{SN,r}(y_{SN})(\tilde{\rho}y_R)^{\nu_R}, \\
&\frac{\partial(y_R)}{\partial\tilde{t}} + \frac{H}{E}\tilde{\nabla}_{\mathbf{x}}\cdot(\tilde{\mathbf{u}}y_R) = \\
&\qquad \frac{1}{Pe_R}\tilde{\nabla}_{\mathbf{x}}\cdot(\tilde{\nabla}_{\mathbf{x}}(y_R)) - Da_{R,r}(y_{SN})(\tilde{\rho}y_R)^{\nu_R},
\end{aligned} \tag{27}$$

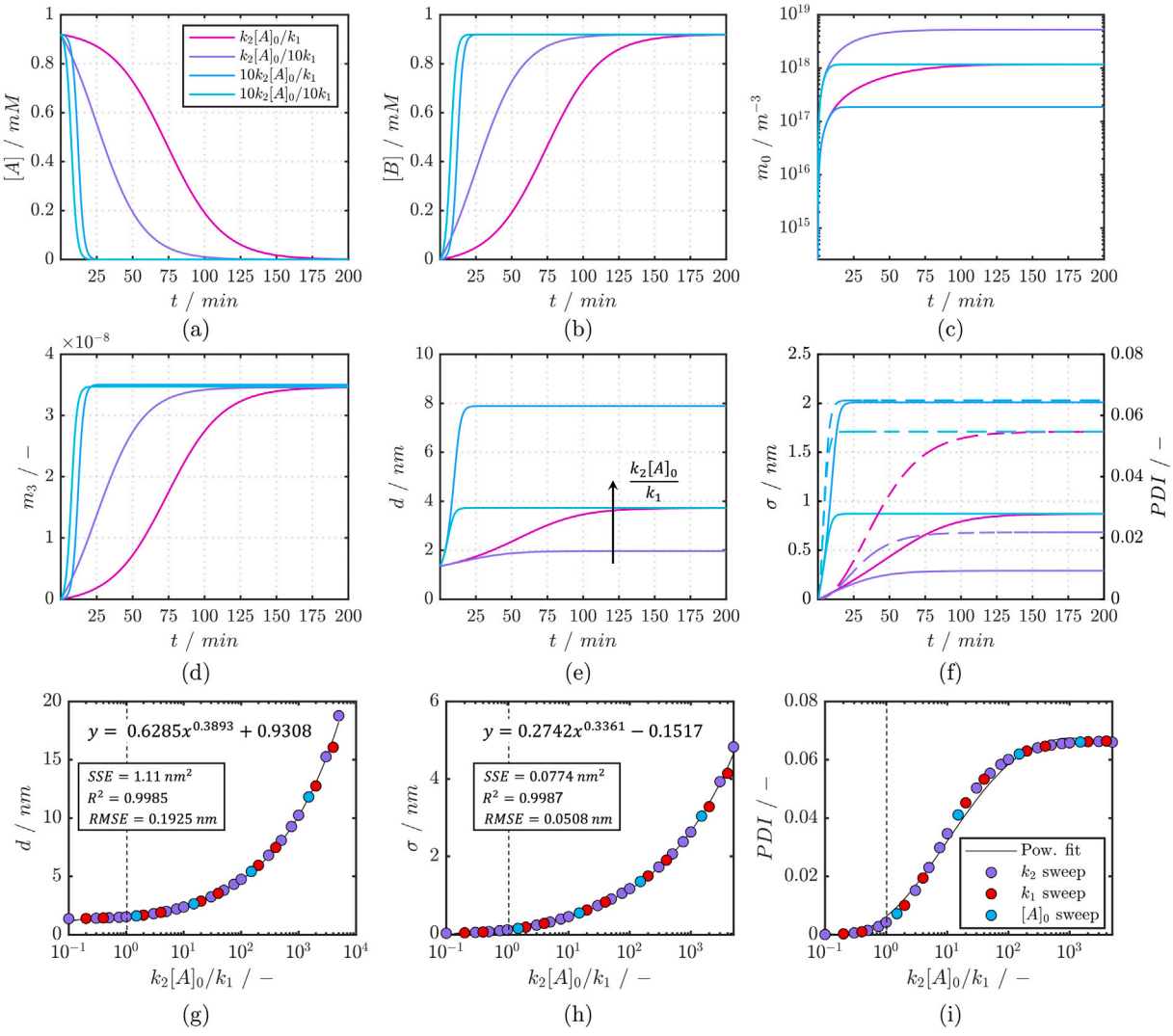

Fig. 5. Effect of the ratio $k_2[A]_0/k_1$ on the PSD in a well-mixed reactor, as predicted by the F–W two-step mechanism. In (a)–(f), the series labelled as '$k_2[A]_0/k_1$' corresponds to the baseline case conditions, whereas the remaining denote one-order-of-magnitude increases of k_1 and k_2 individually and simultaneously. In (f), the continuous line corresponds to σ and the dashed line to PDI. In (g)–(i), we demonstrate the collapse of the d, σ, and PDI curves to a universal dependence on $k_2[A]_0/k_1$ which can be fitted to functions whose parameters are shown in the panel legends. The limit $k_2[A]_0/k_1 < 1$, where F–W is invalid, is highlighted by the vertical dashed line. $[A]_0 = 0.92$ mM, $[TA]_0 = 0.123$ mM, $[B]_0 = 0$ mM, $d_{crit} = 1.35$ nm, $d_m = 0.344$ nm.

where the tildes designate dimensionless variables. The dimensionless groups of Eq. (27) are defined as follows:

$$Pe_{SN} = \underbrace{\frac{U_a}{H}}_{t_{res}^{-1}} \overbrace{\frac{E^2}{D_{SN}}}^{t_{SN,mix}}, \quad Da_{SN,r} = \underbrace{k_r \left(\frac{\rho_c}{MW_R}\right)^{\nu_R}}_{t_{SN,r}^{-1}} \overbrace{\frac{H}{U_a}}^{t_{res}}$$
$$Pe_R = \underbrace{\frac{U_a}{H}}_{t_{res}^{-1}} \overbrace{\frac{E^2}{D_R}}^{t_{R,mix}}, \quad Da_{R,r} = \underbrace{\frac{k_r \nu_R MW_R^{1-\nu_R} \rho_c^{\nu_R}}{MW_{SN}}}_{t_{R,r}^{-1}} \overbrace{\frac{H}{U_a}}^{t_{res}}. \tag{28}$$

In the above, $U_a = (4/\pi)(Q/E^2)$, the average velocity across the channel, and $t_{res} = H/U_a$, the average residence time, correspond to the characteristic velocity and time scales, respectively. In the present context, the Péclet number of species j, Pe_j, can be understood as the ratio between the characteristic time scales of diffusive mixing and flow residence time ($t_{j,mix}/t_{res}$), whereas the Damköhler number of species j, $Da_{j,r}$, provides a dimensionless measurement of the speed of consumption of species j due to the reduction reaction relative to the residence time ($t_{res}/t_{j,r}$). Consequently, a case described by $Pe_j \gg 1$ and $Da_j \gg 1$ is limited by the mixing of the reagents and undergoes a fast reduction process when compared to the residence time of the flow.

In addition to these dimensionless groups, it is instructive to also consider the Reynolds number of our system, $Re = \rho_c U_a E/\mu_c = 4.24 - 16.98$, and the transversal Péclet number of species j, $Pe_{trav,j} = u_x E/D_j = t_{j,mix}/t_{conv}$. This latter number establishes the relationship between the characteristic time of diffusion of j and the time associated with convective mixing, providing an estimate of the contribution of convection to the mixing process. Instead of using Ua, which is predominantly influenced by the velocity component in the y-direction, we define $Pe_{trav,j}$ based on the transversal velocity (i.e., the velocity in the x-direction, as shown in Fig. 1(c)). For our highest flow rate (200 μL/min) and the lowest mass-diffusion coefficient between the inlet streams (D_R), we estimate maximum values of $Pe_{trav,j}$ in the range of approximately 10^{-1} to 10^{-2}. As expected, the contribution of convection to mixing in our system is negligible, and the outcomes of our process are primarily determined by diffusive mixing and its relation to t_{res}. This feature arises due to two main reasons. Firstly, the

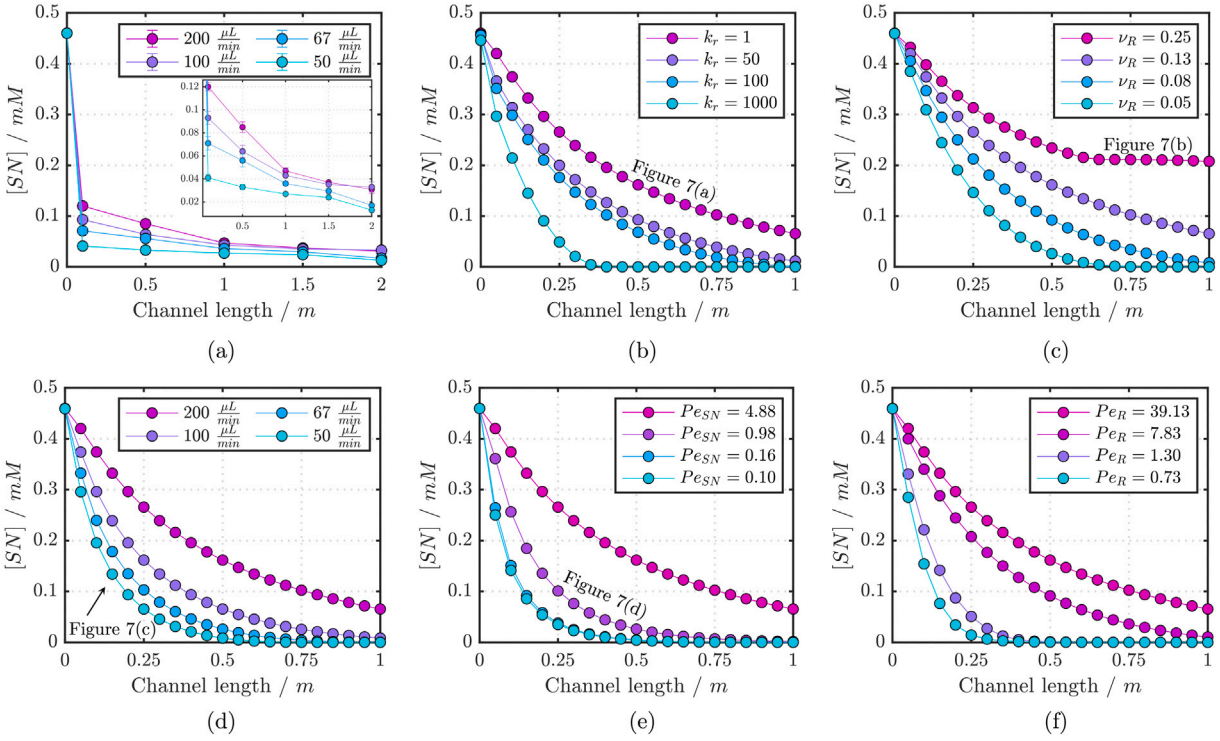

Fig. 6. Influence of hydrodynamic parameters on the steady-state concentration of AgNPs precursor (or silver ions) along the T-junction microchannel. (a) Experimental data measured under different conditions of Q. (b) Effect of k_r (varying $Da_{j,r}$). (c) Effect of ν_R (varying $Da_{j,r}$). (d) Effect of Q (varying $Da_{j,r}$ and Pe_j simultaneously). (e) Effect of Pe_{SN}. (f) Effect of Pe_R. The data points from the simulations correspond to the cell averages over different cross-section planes normal to the y-direction (channel length). All other operating parameters remain unchanged from those specified in Section 2.3 for the base case and the kinetic/dimensionless parameters not mentioned explicitly in the labels of each plot correspond to $k_r = 1$ $\mathrm{m}^{3\nu_R}\,\mathrm{s}^{-1}\,\mathrm{mol}^{-\nu_R}$, $\nu_R = 0.13$, $Pe_{SN} = 4.88$, and $Pe_R = 39.13$.

low Re ($\lessapprox 150$) fully suppress the development of asymmetric vortical structures in the channel cross-section, which are responsible for promoting mixing in microchannels, as demonstrated previously [74]. Secondly, our straight channel geometry eliminates any possibility of generating transversal flows and recirculation patterns, commonly induced by coiled reactors even at low Re [47,75]; additional effects of employing a straight reactor geometry in the context of the PSD are discussed in Section 4.2.2.

Fig. 6(a) portrays the experimentally-measured steady-state concentration of silver ions (silver precursor in solution) across the channel length under different conditions of inlet flow rate and subject to the baseline conditions of pH and reactants concentration (see Section 2.3 and Table 1). We discern a very rapid consumption within the first ~ 0.125 m of the channel, followed by a much slower, almost linear or parabolic consumption until the 2 m mark is reached, where small but non-negligible traces of precursor are detected ($[SN] = 0.031 \pm 0.0036$ and 0.013 ± 0.0013 mM for the highest and lowest flow rates, respectively; see inset of Fig. 6(a)). The rapid precursor consumptions seen across the channel display an inverse response against the inlet flow rate. Lower flow rates give rise to higher residence times whose influence is materialised in higher (lower) $Da_{j,r}$ (Pe_j), promoting the consumption of both SN and R via the reduction reaction, as well as their diffusive transport (see Eq. (27)).

The relationship between precursor consumption and inlet flow rate found experimentally is reproduced via the numerical simulations, as depicted in Fig. 6(d). We make the note that all simulation results shown in this set of plots, in conjunction with those of Fig. 7, were run for a total channel length of 1 m due to the extensive computational resources required to capture the entire 2 m domain; as seen from the experimental profiles, the zones where most phenomena of interest take place are well within the first 1 m of the channel. The intensification of precursor consumption per channel length seen at lower flow rates triggers a similar effect on the formation of silver atoms ($Ag_{(l)}$) available for nucleation and growth, which, as will become apparent in the following discussions, have major consequences on the PSD and its spatial distribution within the channel. Yoo et al. [76] and Iwamoto et al. [77] have suggested that variations in the rate of the reduction reaction in particular bring about prominent changes to the evolution of the subsequent reactions and the final PSD for AuNPs. Accordingly, Fig. 6(b) illustrates the effect of the reduction kinetic constant for our system using the stoichiometric conditions and transport properties that correspond to those of TA for the reducing agent, as stipulated in Section 3.2. Expectedly, increasing k_r under the concentration conditions of the reducing agent ($\nu_R = 0.133$ and $[R]_{inlet} = 0.123$ mM) increases the rate of SN consumption across the channel (increased $Da_{j,r}$) until a virtually total consumption before 1 m is seen at $k_r > 100$ $\mathrm{m}^{3\nu_R}\,\mathrm{s}^{-1}\,\mathrm{mol}^{-\nu_R}$.

Fig. 6(c) shows that the precursor consumption is also heavily linked to the stoichiometric conditions of the reduction reaction between SN and a potential TA-TC complex. It is observed that ν_R inversely generates higher rates of SN consumption per reactor length, explained by the accentuation of the 'excess' effects concerning the concentration of the reducing agent (0.123 mM) and its imbalance against that of SN (0.92 mM). Therefore, as ν_R increases to reach a critical value located in the range $0.133 - 0.25$, R begins to be consumed at a decidedly faster rate than SN, as evidenced by the non-zero constant profile of $[SN]$ beyond 0.6 m from the inlet at $\nu_R = 0.25$, indicating now an excess concentration of SN.

To finalise this part of the discussion, we plot in Fig. 6(e)–(f) the profiles of precursor concentration obtained by varying Pe_j and maintaining all other dimensionless numbers and reaction parameters unchanged from the ones specified in the caption of the figure; the variations of Pe_j were made by altering the values of the mass diffusion coefficients of species $j = SN, R$. This set of results clearly exemplifies the coupled and interdependent effects of flow hydrodynamics and reaction kinetics that govern the synthesis of AgNPs. As Pe_j decreases

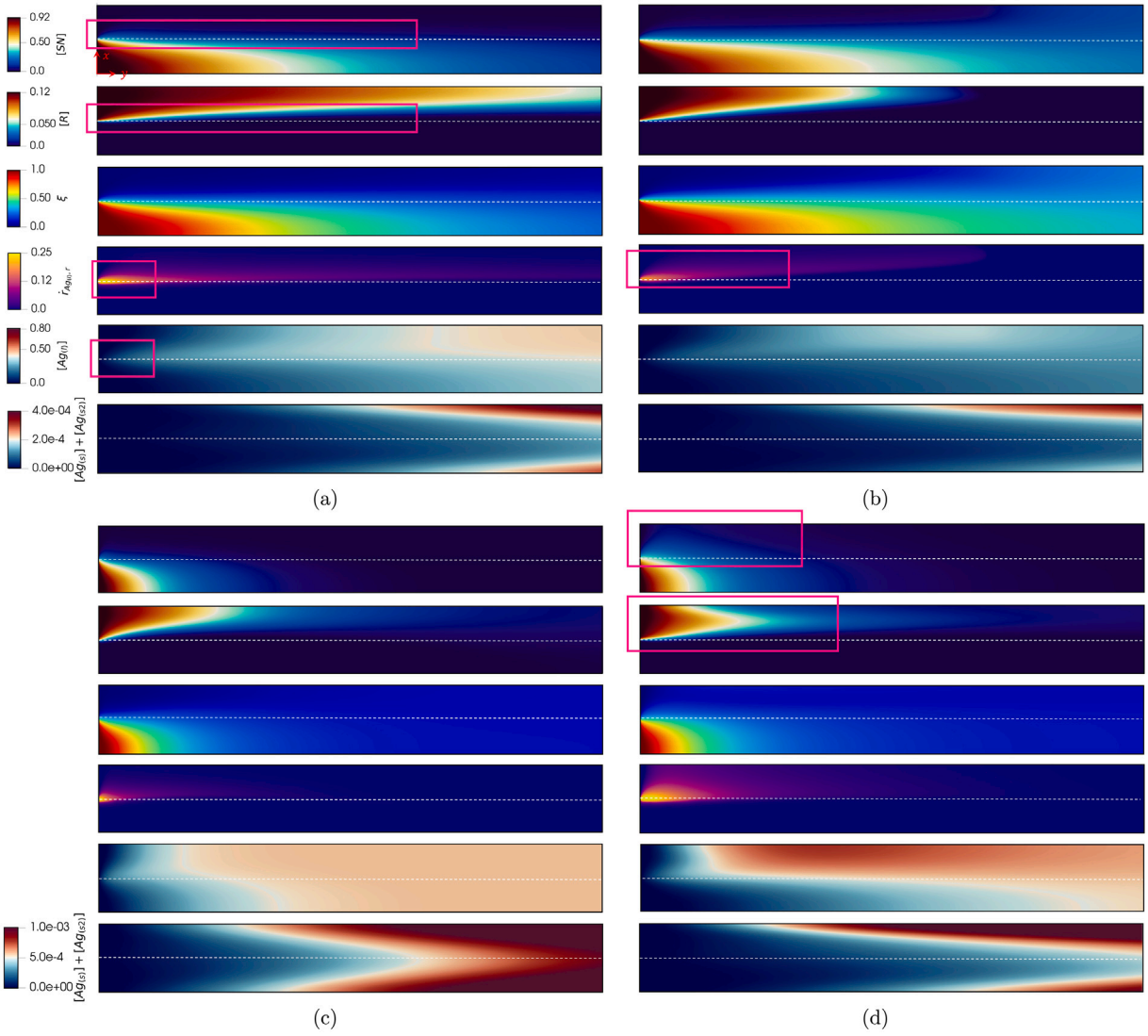

Fig. 7. Steady-state simulation contour profiles in the T-junction microchannel for $[SN]$ in mM, $[R]$ in mM, ξ, $\dot{r}_{Ag_{(l)},r}$ in $\mathrm{mMs^{-1}}$, $[Ag_{(l)}]$ in mM, and $[Ag_{(s)}] + [Ag_{(s2)}]$ in mM (top to bottom, respectively). (a) $k_r = 1\ \mathrm{m^{3\nu_R}\,s^{-1}\,mol^{-\nu_R}}$, $\nu_R = 0.133$, and $Q = 200$ μL/min ($Da_{j,r} = 68.78, 91.60$ and $Pe_j = 4.88, 39.13$ for SN and R, respectively). (b) $\nu_R = 0.25$ ($Da_{j,r} = 2.55 \times 10^4, 3.63 \times 10^2$ for SN and R, respectively). (c) $Q = 50$ μL/min ($Da_{j,r} = 1.22, 9.78$ and $Pe_j = 2.75 \times 10^2, 3.66 \times 10^2$ for SN and R, respectively). (d) $Pe_{SN} = 0.98$. All other operating parameters remain unchanged from those specified in Section 2.3 for the base case and all kinetic/dimensionless parameters not mentioned in the captions of each figure correspond to those of (a). For easier visualisation, the inlet streams of all contour plots have been removed and the channels have been rescaled from their original dimensions as follows: $\mathbf{x} = (25x, 0.1y, z)$.

(D_j increases), we find a much higher consumption of SN per reactor length given the faster mixing of the reactants and its concomitant accelerated reduction kinetics within the region 0–0.25 m (see last term on the RHS of Eq. (27)).

The parametric sweep examined above has demonstrated the strong influence of flow hydrodynamics on the evolution of the chemical reactions involved in the system. We expand on these concepts through Fig. 7, where we display the steady-state contour plots of a few relevant variables across the T-junction microchannel. From top to bottom, these variables are: $[SN]$, $[R]$, ξ, $\dot{r}_{Ag_{(l)},r}$, $[Ag_{(l)}]$, and $[Ag_{(s)}] + [Ag_{(s2)}]$. In this context, $\xi = \frac{[SN]-[R]+[R]_{inlet}}{[SN]_{inlet}+[R]_{inlet}}$ corresponds to the mixture fraction, which provides a quantitative measure of the degree of mixing of two flow streams ($\xi = 1$ for pure SN, $\xi = 0$ for pure R, and $\xi = 0.5$ for a well-mixed and non-reacted feed) [69]; $\dot{r}_{Ag_{(l)},r} = k_r[SN][R]^{\nu_R}$ is the rate of $Ag_{(l)}$ production (in mM) due to the reduction reaction (see Eq. (18)). The dashed white line on each contour marks the channel centre-line normal to the x-direction ($x/E = 0.5$, see the location of Cartesian axis)

The case shown in Fig. 7(a), whose $[SN]$ profile is labelled in Fig. 6(b), exemplifies the comparatively faster consumption of SN obtained as a result of the reaction stoichiometry ($\nu_R = 0.133$ and $7.5 : 1$ $[SN]_{inlet} : [R]_{inlet}$), whereby SN shows a steep concentration decline before reaching the channel centre in the length-wise direction ($y/H \sim 0.5$ m) whilst, for the most part, $[R] > 0.05$ mM on its side of the channel ($x/E > 0.5$) throughout the entire length domain. Although not explicitly shown in the figures, we report for this case that around 7.12% of the inlet concentration of SN is left at the outlet, compared to the 13.32% of its R counterpart. This unbalanced consumption of the two main reagents notably limits the production of $Ag_{(l)}$, the size of the particles, and the outlet sample's concentration of AgNPs, as explained in the following subsection. The contours of ξ, $\dot{r}_{Ag_{(l)},r}$, $[Ag_{(l)}]$, and $[Ag_{(s)}] + [Ag_{(s2)}]$ for this case reveal the existence of small localised regions of perfect mixing ($\xi = 0.50$) in the vicinity of $x/E = 0.50$ and close to the T-junction in the y-direction, where $\dot{r}_{Ag_{(l)},r}$ reaches its maximum value (see highlighted zone). Downstream from this region, the fast consumption of SN induces a rapid drop in $\dot{r}_{Ag_{(l)},r}$ and an appreciable distortion of the zones described by $\xi = 0.50$.

In Fig. 7(a) we detect a stark difference in the location of the accumulation zones of $Ag_{(l)}$ (channel centre in x and towards the outlet)

versus those of Ag_s and Ag_{s2} (near the channel walls). This observation is a clear indication of the timescale disparity related to the phenomena of reduction and nucleation/growth and how each one compares to t_{res}. For this case, $t_{res} \sim 29$ s, $t_r \sim 0.30 - 0.40$ s, $t_{nuc} = 1/k_1 = 5.45 \times 10^4$ s, and $t_g = 1/k_2[Ag_{(l)}]_{max} = 1.18 \times 10^3$ s (i.e., $t_r < t_{res} < t_g < t_{nuc}$). The fast reduction step induces an almost immediate formation of $Ag_{(l)}$ at the centre of the channel (where $\xi = 0.5$), as seen in the highlighted section of the $[Ag_{(l)}]$ contour, that leads to an eventual $[Ag_{(l)}]$ accumulation in the areas surrounding the outlet. In contrast, the much slower nucleation and growth steps restrict the formation of $Ag_{(s)}$ and Ag_{s2} to the regions where the local residence time is large enough for those processes to take place (near the channel walls) and where the concentration of $Ag_{(l)}$ is sufficiently high (the channel outlet).

By exploring the concentration of SN and R beyond the side of their individual inlet in the x-direction (i.e., exploring $x/E > 0.5$ for SN and $x/E < 0.5$ for R), one can discern a higher SN 'crossover' to the side of R, as highlighted in the contour plots. We rationalise these findings by linking them to the mass diffusivity coefficients of SN and R (and Pe_j). The higher diffusivity of SN (lower Pe) allows it to cross the centre-line at a faster rate than R, providing an explanation for the residual SN at $x/E > 0.5$ and the preferential formation of $Ag_{(l)}$ towards those regions in the channel.

The repercussions of $D_{SN} > D_R$ become particularly noticeable as ν_R is increased to reach the domains of excess SN (total exhaustion of R), as depicted in Fig. 7(b), where it is seen that the presence of SN extends over the entire channel diameter as we approach the channel outlet. This mass diffusivity disparity between SN and R is also responsible for the spatially uneven development of the high $\dot{r}_{Ag_{(l)},r}$ trail that emerges from the hot spot close to the T-junction (see figure highlight). As previously remarked, the longer flow residence that characterises an operation with lower flow rates promotes the consumption of both SN and R due to an increased (decreased) $Da_{j,R}$ (Pe_j). These effects can be appreciated in the contour plots of Fig. 7(c) for $Q = 50$ μL/min, where both species are nearly consumed before reaching the channel half point. The rapid consumption of both reagents, in addition, increases the overall production of $Ag_{(l)}$ per channel length and thus that of $Ag_{(s)}$ and $Ag_{(s2)}$ (notice the colour bar scale of the latter two species in comparison to that of Fig. 7(a)–(b)). These higher residence times are also responsible for the effectively homogeneous distribution of $[Ag_{(l)}]$ after $y/H \sim 0.5$.

Fig. 7(d) describes how a reduction in Pe_{SN} from a rise in D_{SN}, in addition to accentuating the radial disparity in the concentration profiles of SN and R (see highlights), considerably increases $\dot{r}_{Ag_{(l)},r}$, $[Ag_{(l)}]$, and $[Ag_{(s)}]$ compared to, for example, Fig. 7(a). This is due to a higher SN crossover to the realms of $x/E > 0.5$, which consequently triggers higher mixing and reaction rates. The steady-state profiles of SN along the channel that correspond to the cases of Fig. 7(c) and (d) (Fig. 6(d) and (e), respectively) suggest similar overall amounts of SN consumed and $Ag_{(l)}$ produced (not shown explicitly here). However, the $[Ag_{(l)}]$ contour of Fig. 7(d) depicts a notably more uneven spatial distribution of this species, an observation likely caused by the larger D_{SN}/D_R ratio of this case compared to that of Fig. 7(c).

4.2.2. Effect of hydrodynamics on the PSD of AgNPs

The previous subsection provided a detailed illustration of the underlying phenomena governing the synthesis of AgNPs from the perspective of hydrodynamic and kinetic time-scale competitions and their notable influence on the consumption of reactants/production of nanoparticles. This subsection links these experimental and simulation findings to the PSD of the samples in the T-junction microchannel and thoroughly describes the spatial distribution of the variables involved in the process along the channel.

Fig. 8(a)–(c) present the experimentally-measured steady-state PSD across different channel lengths and for different inlet flow rates, with the summarised results reported in the table insets of each figure; as is the case throughout this investigation, the remaining operating conditions are those assigned to the base case. These figures elucidate the strong connections between flow hydrodynamics and PSD, whereby for all channel lengths the average particle size and its standard deviation undergo a monotonic decrease with the increase of inlet flow rate. Barring the outlier measurements at 1 m and $Q = 200$ μL/min, both d and σ appear to follow an almost-linear trend against the channel length; the slopes of these functions also exhibit a negative response to the flow rate (d slope $\sim 5.38, 5.33, 5.04$ and σ slope $\sim 2.11, 1.79, 1.53$ nm/m for $Q = 50, 100, 200$ μL/min, respectively). Interestingly, the PDI does not appear to show a clear monotonic response against either the channel length or the flow rate, but in all cases (except for $Q = 50$ μL/min at 2 m) is within an acceptable range for a monodispersed sample ($PDI \lesssim 0.10$) [78]. The simulation results of Fig. 8(d)–(f) adhere to the same inverse relationship between flow rates and PSD and depict a similar semi-linear evolution of d and σ across the channel domain as the experiments. We note that these simulation results are reported for a shorter channel length (0.25 m) due to the prohibitively large computational resources needed to resolve the dynamics of the full channel, which is left for future work. The above results are entirely consistent with previous investigations of similar systems, where experiments have demonstrated that the hydrodynamic conditions of laminar microreactors exert a major influence over the PSD [15,79]. The variation in residence time brought about by modifying, for instance, the operating flow rate has been determined to be one of the main factors that alter the PSD and the shape of the NPs. Ling et al. [80] and Aljarrah et al. [81] have examined the effect of residence time on the morphology of silica and gold NPs, respectively, and have reported that shorter residences times lead to smaller size distributions.

The crucial differences in the dynamics that transpire going from a well-mixed reactor to a continuous-flow microchannel are evident when comparing the sizes reported in Fig. 8 to those in Fig. 4(a) (and Table 2) under the same conditions of pH and $[TC]_0$. The approximately tenfold increase in both d and σ seen by synthesising AgNPs in a microreactor is a clear depiction of how hydrodynamics, kinetics, and PSD are closely intertwined. Herein, we elucidate the explicit interrelations between these phenomena and contextualise them in terms of the differences between the F–W mechanism for well-mixed reactors and our extension for microfluidics.

In a well-mixed reactor, the attainable particle sizes are strictly constrained by both the availability of precursor A for direct conversion into B (see Eqs. (1)–(2)) and the interplay between nucleation and growth. This constraint arises from the fact that the F–W expressions employed to simulate these phenomena (Eqs. (13)–(14)) are direct functions of $[A]$ and are mediated by the relation between nucleation and growth (as demonstrated in Fig. 5). In a well-mixed system the consumption process of A proceeds continuously and without delays caused by transport phenomena. Consequently, the "fast" and "direct" consumption of A into B limits the particle sizes that can be reached. In contrast, reactions in microchannels are governed by the very slow convective/diffusive dynamics ($Re = 4.24 - 16.98$ in our system) responsible for mixing the initially-separated reactants streams. These slow and controlled processes, in addition to delaying precursor consumption, facilitate particle agglomeration events that lead to larger particles. From these remarks, we can envision the well-mixed reactor as the limit where the onset of precursor consumption occurs almost immediately after the start of the operation (i.e., no reaction delays stemming from mixing) and where particles do not have enough time to aggregate in the reactor.

The above discussion serves as an additional explanation of the inverse relationship observed between outlet particle sizes and inlet flow rates. As the flow residence time decreases with an increase in the flow rate, both the simulations and the experiments suggest a reduction in the consumption of the precursor per reactor length (see the discussion of Figs. 6–7). This in turn critically diminishes the production of $Ag_{(l)}$, the driving force for nucleation and growth (see

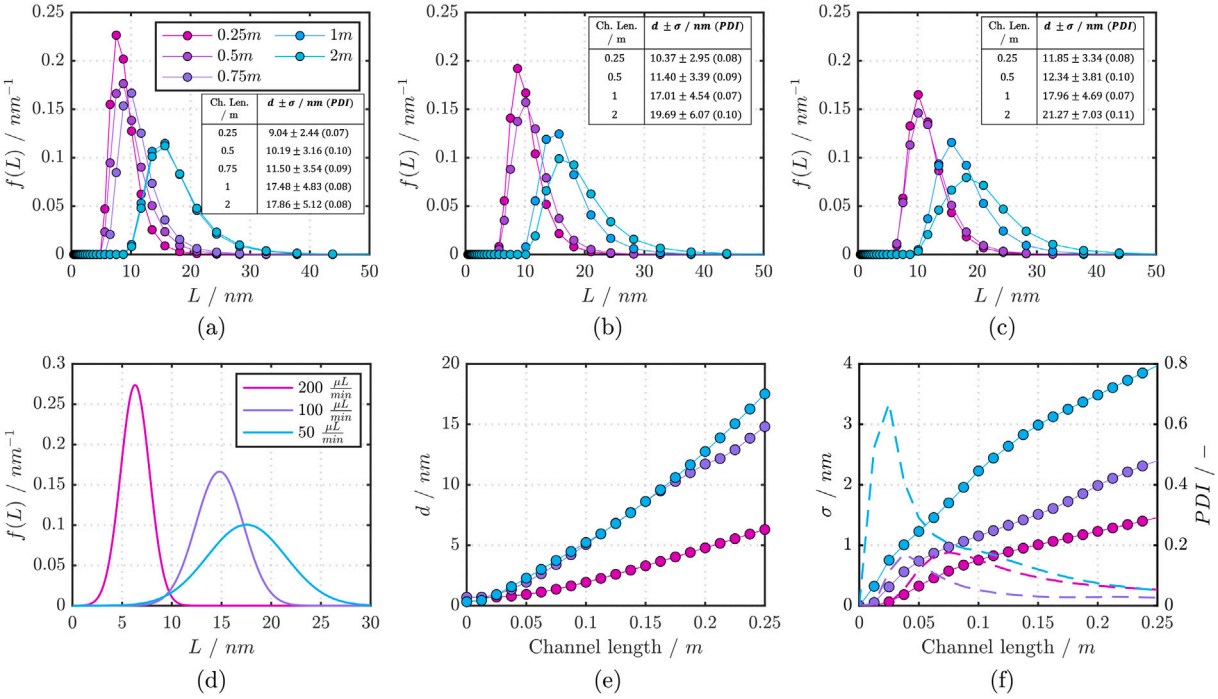

Fig. 8. Influence of inlet flow rate on the PSD along the T-junction microchannel. (a)–(c) Experimental data measured at different outlet channel lengths for (a) $Q = 200$ μL/min, (b) $Q = 100$ μL/min, and (c) $Q = 50$ μL/min. (d) Steady-state PBM-CFD PSD obtained at an outlet length of 0.25 m. (e) Steady-state PBM-CFD average diameter along the channel length. (f) Steady-state PBM-CFD standard deviation (left axis, marks) and PDI (right axis, dashed line) along the channel length. The data points in (e) and (f) correspond to the cell averages over different cross-section planes normal to the y-direction. All other operating parameters remain unchanged from those specified in Section 2.3 for the base case. For these cases, $k_r = 1000$ m$^{3\nu_R}$ s^{-1} mol$^{-\nu_R}$, $\nu_R = 0.05$, $d_{crit} = 0.7$ nm, and $d_m = 0.344$ nm. These reacting parameters have been selected as they better adhere to the excess conditions of the reducing agent in the experiments, as well as the reduction time ($\sim 3.9 \times 10^{-4}$ s) suggested in the literature [56]. The dimensionless numbers and characteristic times that describe these cases, in order of decreasing Q, are: $t_{res} \sim 7.36, 14.72, 29.45$ s, $Da_{SN,r} = 1.01\times10^4, 2.03\times10^4, 4.05\times10^4$, $Da_{R,r} = 5.07\times10^3, 1.01\times10^4, 2.03\times10^4$, $Pe_{SN} = 1.95\times10^1, 9.76, 4.88$, $Pe_R = 1.57\times10^2, 7.88\times10^1, 3.91\times10^1$. For all three cases, $t_{SN,r} \sim 7.27\times10^{-4}$ s, $t_{R,r} \sim 1.45\times10^{-3}$ s, $t_{SN,mix} \sim 1.43\times10^2$ s, $t_{R,mix} \sim 1.15\times10^3$ s, $t_{nuc} \sim 5.45\times10^4$ s and $t_g \sim 1.18\times10^3$ s.

Eqs. (19)–(20)). The combination of an overall lower concentration of $Ag_{(l)}$ available for nucleation and growth, along with a shorter time for agglomeration, explains the smaller particle sizes observed at higher flow rates.

In our system, the use of microfluidics permits the synthesis of larger-sized NPs with equal or even higher-size monodispersity, as seen from the PDI values. The work of Wu et al. [75] has established similar connections between mixing rates and residence times with the PSD by analysing different microreactor geometries. A key finding from that work is the significant reduction in particle size obtained via operations with helical microreactors, whose curved domains allow for the development of secondary transversal flows that aid in the mixing of the reagents, reducing the radial-wise variability in species concentration and promoting a rapid consumption of the precursor and NP nucleation. We confirm these findings in the additional set of experiments detailed in section 3 of SI, figure S4, where we compare the outlet PSD of our straight reactor with that of a coiled geometry; under the same conditions of Q and pH, the coiled reactor provided an enhanced convective mixing process, resulting in smaller particles.

We now proceed to analyse the spatial distributions of a few relevant PBM-related variables within the T-junction microchannel; these distributions clearly encapsulate and summarise the connections between hydrodynamics, reaction kinetics, and PSD. Fig. 9(a)–(c) portray the steady-state snapshots of m_0, m_3, and d for the three flow rates tested. We complement these contours with the plots of Fig. 9(d)–(i), which depict the radial-wise profile of each variable at the outlet plane of the channel (normal to the y-direction). As expected from our previous findings related to $[Ag_s + Ag_{s2}]$ in Fig. 7, the volume fraction of the dispersed phase ($\phi_d \sim m_3$) preferentially accumulates at the vicinity of the walls, where, on average, the particles are also much larger than at the centre-line. Recalling our statements about the critical effects associated with the residence time in the channel, it is unsurprising that the largest-sized particles tend to gather near the channel walls, where the lowest flow velocities are found (Fig. 9(d)) and, consequently, the particles have a longer time to grow from nuclei, agglomerate, and deposit, leading to a higher ϕ_c. As seen from the contour plots and the outlet profiles, these outcomes are heightened by operations with lower flow rates, whereby a cascade of coupled kinetic and hydrodynamic events, driven by higher residence times, give rise to larger AgNPs and higher NPs volume fractions. Namely, longer residence times initially lead to an accelerated precursor consumption per reactor length (see $[SN]$ outlet profile, Fig. 9(h)), which promotes the production of $Ag_{(l)}$ close to the inlets and therefore the generation and growth of small-sized nuclei. The increased time span in which nucleation and growth are allowed to take place eventually generates high rates of $Ag_{(l)}$ consumption at low Q, which virtually equalise the average $[Ag_{(l)}]$ at the outlet plane between the highest and lowest Q (Fig. 9(i)). These events, in conjunction with inter-particle agglomeration instances (which are boosted by particle size, see Eq. (26)) finally bring about the noteworthy differences in particle size we observe between varying flow rates.

The effects of flow residence time on the balance between nucleation, agglomeration, and particle diffusion are manifested in the appreciably more homogeneous m_0 (number of particles density) outlet radial profiles at lower flow rates, despite similar surface-averaged values over this plane ($1.81, 2.28, 2.52 \times 10^{19}$ m^{-3} for $Q = 200, 100, 50$ μL/min, respectively). Under high Q conditions, the particles tend to accumulate close to the walls and disproportionately towards one side of the channel given the uneven radial distribution of $[Ag_{(l)}]$ (refer to our analysis of Section 4.2.1, Fig. 9(i)). These axial heterogeneities diminish at lower flow rates via diffusive transport of $Ag_{(l)}$, the nuclei, and the AgNPs themselves. Interestingly, Fig. 9(a,e) show that the preferred zones of m_0 accumulation in the radial direction do not correspond to the vicinity of the walls, as it is the case of d and m_3 (Fig. 9(f–g)); instead, the particle accumulation areas are shifted towards the

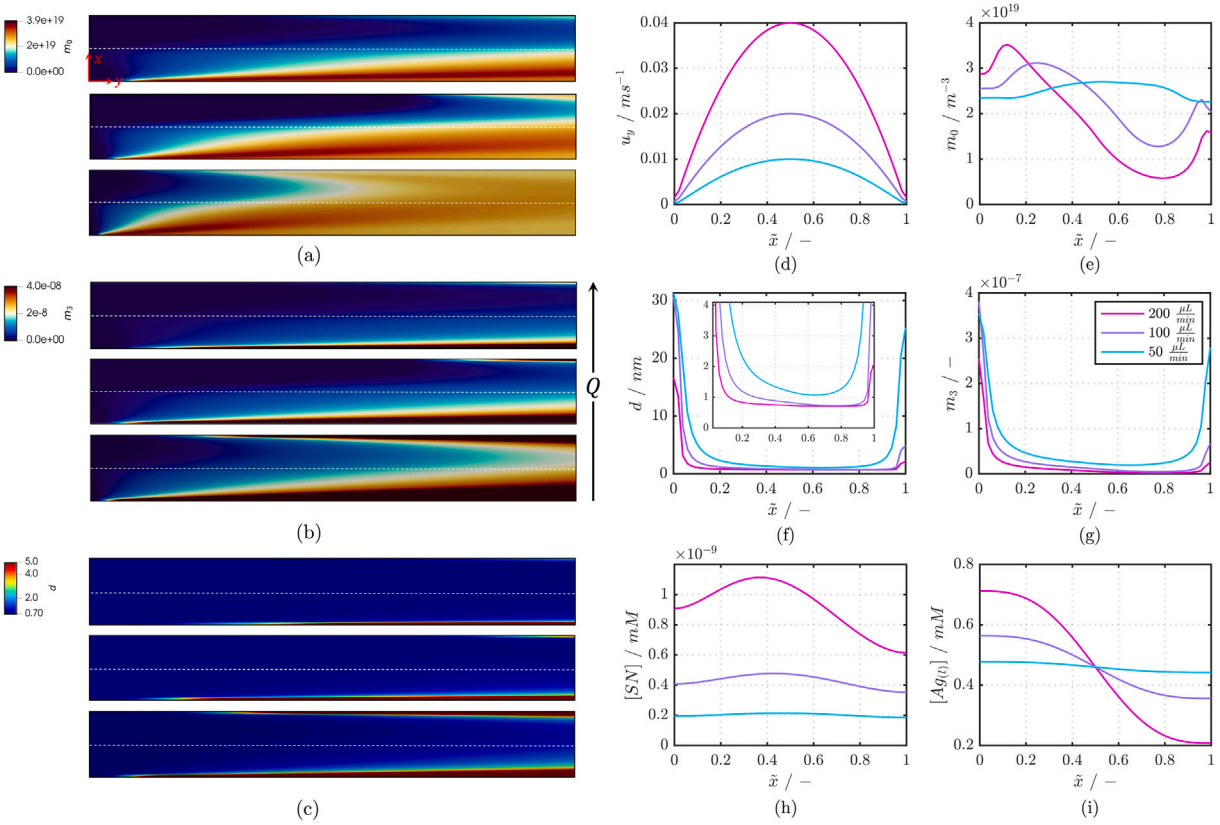

Fig. 9. Influence of inlet flow rate on the spatial distribution of AgNPs in the T-junction microchannel. (a)–(c) Steady-state contour plots of m_0 in m^{-3}, m_3, and d in nm, respectively. From top to bottom: $Q = 200, 100, 50$ μL/min. (d)–(i) Steady-state radial distributions of the variables at the outlet plane for a channel length of 0.25 m. All other operating parameters remain unchanged from those specified in Section 2.3 for the base case. For these cases, $k_r = 1000$ $m^{3\nu_R}$ s^{-1} $mol^{-\nu_R}$, $\nu_R = 0.05$, $d_{crit} = 0.7$ nm, and $d_m = 0.344$ nm. See the caption of Fig. 8 for the characteristic times and dimensionless numbers for each flow rate case. The scale colour bar of d is set from d_{crit} to 5 nm for a clearer depiction of the profiles, refer to (f) for the real values. For easier visualisation, the inlet streams of all contour plots have been removed and the channels have been rescaled from their original dimensions as follows: $\mathbf{x} = (7x, 0.1y, z)$.

channel centre. This suggests instances of dominant agglomeration over nucleation events at the locality of the walls, whereby the rapid rates of nucleation induced by high $[Ag_{(l)}]$ are not sufficient to overcome the rates of agglomeration, resulting in lower m_0. Looking at the overall picture, a similar but opposite remark can be made about the influence of the flow rate on m_0, where the surface-averaged values over the outlet plane slightly increase with a Q decrease. Considering the higher rates of both nucleation and agglomeration per channel length at Q = 50 μL/min, the fact that m_0 is still higher on average than at Q = 200 μL/min appears to be an indication of dominant particle-creation nucleation events over m_0-destructive agglomeration instances.

At this point, we draw attention to the fact that our F–W-based PBM-CFD simulations provide useful and acceptable quantitative predictions of d and σ in the microreactor and, as mentioned before, are able to correctly capture the overall phenomena involved in the reacting system, especially in terms of operation-driven variations in d and σ and their distributions as the flow evolves along the channel. We attribute the quantitative deviations from the experiments to three main limitations of our model. The first one corresponds to the uncertainty regarding the reduction reaction and the role/properties of the TA-TC complex, both of which influence the rate of precursor consumption and thus the PSD of the sample in a pronounced manner, as seen in Fig. 6(b)–(c). The second factor is related to using the F–W two-step mechanism – originally designed for a well-mixed system – as the basis for modelling the continuous-flow microreactor. Even though our proposed model extensions take into account the diffusive and convective mixing effects not explicitly accounted for in the F–W mechanism, certain incompatibilities between the two systems may exist. For instance, we note that the kinetic constant k_1 describing nucleation, as it is proposed, already takes into account every step leading up to nucleation, including the reduction reaction, which we model separately. In addition, we highlight that the numerical results at the lower flow rates feature apparent over-predictions of particle size in the range 30−40%, whilst the data points at Q = 200 μL/min correspond to under-predictions. From this observation, it can be inferred that our simulations overestimate the effects of higher residence times, which likely stems from overly-magnified agglomeration events, which were modelled through a purely hydrodynamic agglomeration kernel (Eq. (26)). As an avenue for future work, it is proposed to add an agglomeration efficiency term to the PBE (see Eqs. (25)–(26)) that explicitly correlates inter-particle (see SI, figure S5) and particle-stabiliser interactions [68] at the molecular level to an agglomeration efficiency per collision event, similar to that employed in Bal and Bandyopadhyaya [37]. The third factor corresponds to the deviations inherent to the F–W two-step mechanism in predicting the system's temporal evolution in well-mixed environments, as mentioned in the literature review of Section 1 and discussed from our results of Section 4.1, whose deviations are presumably carried over to the T-junction simulations. We also highlight that, as opposed to the circular cross-section geometry of the channel in the experimental setting, the simulation domain corresponds to a simplified 2-D version of the channel. This feature might trigger small but non-negligible differences in the mixing process, which, as seen throughout the manuscript, have a direct influence over the PSD and may contribute to the deviations found. A final restriction of our model worth mentioning corresponds to its current limitation to continuous-flow microfluidic operations, which represent highly-diluted reactive single-phase flows. Adapting the computational model to cover droplet-based synthesis in microfluidics introduces additional

complexity, necessitating a robust framework to capture the intricate interfacial phenomena that characterise reactive liquid–liquid flows; this topic is also suggested for future work as interesting comparisons could be made between the performance of droplet-based microfluidics and that of continuous-flow systems with coiled reactors.

5. Conclusions

This work presents an exhaustive examination of the underlying phenomena dictating the chemical synthesis of AgNPs in a continuous-flow microchannel and a well-mixed batch reactor via experimental and numerical approaches. We propose a coupled PBM-CFD framework to extend the reach of spatially-averaged, time-dependent-only models, such as the well-established Finke–Watzky (F–W) two-step mechanism [28], to cover the highly interdependent dynamics inherent to continuous-flow and non-premixed reacting environments, such as microfluidic channels.

The synthesis of silver and similar nanoparticles (NPs) poses significant challenges from a modelling perspective given its incompatibility with the much better-understood crystallisation- and precipitation-based production of other types of NPs, which typically involves fast supersaturation-driven nucleation events and diffusion-limited growth models [37,40]. Contrastingly, the synthesis of AgNPs is a multi-step interacting process based on the reduction of a silver precursor into Ag atoms, whose concentration serves as the driving force behind a controlled nucleation process and a rapid growth step. To the best of the authors' knowledge, this is the first implementation in open-source code of the coupling between the hydrodynamic and reactive aspects of the system with a population balance model to predict the size distribution of the NPs, elucidate the mechanisms by which the operating conditions influence it, and compare the dynamic events governing microfluidic production to those of well-mixed batch reactors.

Despite certain deviations, which are discussed in detail, the F–W model is able to reproduce in an excellent manner the overall dynamics and qualitative experimental trends regarding pH, stabiliser concentration, and average particle size. In fact, the F–W-based simulations allowed us to summarise the influence of pH and initial stabiliser concentration on the size distribution by way of a unique parameter that decisively determines the final average particle size, the standard deviation of the distribution and consequently, the polydispersity index. This parameter corresponds to the ratio between the initial timescales of nucleation and growth, expressed in terms of kinetic constants as $k_2[A]_0/k_1 = t_n/t_g$ [28], whose value can be directly correlated to the size of the particles through a power-law functional form (see Fig. 5). As such, we understand the notably smaller AgNPs obtained at high pH as simply the product of a promoted nucleation process ($k_2[A]_0/k_1 < 1$) that utilises the available precursor concentration to generate a large number of small nuclei instead of increasing their size via growth events, leading to a fast exhaustion of the precursor, severely restricted growth, and small particle sizes; opposite arguments can be given for cases characterised by $k_2[A]_0/k_1 > 1$.

Our experimental and simulation results for the continuous-flow microchannel unveiled a strong coupling between the system's hydrodynamics, multi-reaction kinetics, and the number and size of the particles. Through dimensionless and time-scale analyses, we showcased how differences in the operating conditions, particularly in the inlet flow rates, in conjunction with the transport properties of the reactants, give rise to varied rates of precursor consumption per reactor length due to alterations in the time-scale ratios between flow residence, reactants mixing, and the reduction reaction. The effects of these varied rates of precursor consumption are carried over to the outlet PSD of the samples through a series of complex steps involving the balance between the creation of Ag atoms and their consumption in nucleation/growth, and between the surge in the number of particles density through nucleation and their decline by means of agglomeration and diffusion.

In spite of the key role our T-junction PBM-CFD simulations played in rationalising the experimental trends observed, we emphasise the discrepancies found between their predictions of average particle size and the experimentally-measured values, which tend to over-estimate the effects of a diminished inlet flow rate. Hence, as avenues for future research, we propose the implementation of an agglomeration efficiency kernel to modulate the number of successful collisions based on molecular interactions between the NPs, and a further examination of the role of the tannic acid-trisodium citrate complex in the reduction of silver nitrate. Moreover, it is crucial to emphasise that our PBM-CFD framework, which builds upon the well-established F–W mechanism and incorporates extensions for microfluidic channels, shows great potential in modelling reduction-based synthesis processes, including IrNPs and AuNPs. Nevertheless, it is imperative to conduct further testing to verify the applicability and reliability of the presented computational framework, as well as to validate the findings of this study. As an immediate next step, we propose testing the model using an alternative chemical synthesis protocol for AgNPs in both well-mixed and microfluidic channels.

The present investigation exemplifies the value and potential of synergistically integrating a robust synthesis setup, such as microfluidics, with a realistic computational model. This combination facilitates the enhancement of existing NP production methods by providing a deeper understanding of the system's underlying phenomena and connecting them to the final properties of the NPs. On the one hand, the experimental work provides a strong foundation for the computational model's assumptions, quantitative estimations of kinetic parameters that can be directly used in the simulations, and benchmarking data. On the other hand, the simulations rationalise the experimental findings, unveiling non-intuitive and experimentally-inaccessible links between the most crucial variables of the system. The thorough analyses conducted on the relevant spatiotemporal scales of the problem and the dimensionless relationships conceptualised via the simulations (e.g., $k_2[A]_0/k_1$, Pe_i, $Da_{i,rxn}$, see Sections 4.1 and 4.2.1) introduce an element of generality to our findings, which can be leveraged for production scale-up. As previously proposed [82], parallelised networks of microfluidic devices can significantly increase production output to potentially reach industrial-scale operations. Such a network requires high levels of connectivity between devices, substantial automation, as well as highly optimised operation at the level of individual microchannels. For this, our combined experimental and computational framework provides a stepping-stone to advance the understanding of reduction-based synthesis in microfluidics.

Declaration of competing interest

The authors declare that they have no known competing financial interests or personal relationships that could have appeared to influence the work reported in this paper.

Data availability

No data was used for the research described in the article.

Acknowledgements

The authors gratefully acknowledge the support from the Engineering & Physical Sciences Research Council, UK, through the PREMIERE Programme Grant EP/T000414/1. The Ph.D. studentship of P.P. is supported by Imperial College London and the Colombian Ministry of Science, Technology and Innovation (MINCIENCIAS). The Ph.D. studentship of K.N. is funded by University of Birmingham. O.K.M. acknowledges the Royal Academy of Engineering for a Research Chair in Multiphase Fluid Dynamics. The authors also acknowledge the HPC facilities provided by the Research Computing Service (RCS) of Imperial College London. The visualisations of the simulation results were generated using Paraview.

Appendix A. Supplementary data

Supplementary material related to this article can be found online at https://doi.org/10.1016/j.cej.2023.145692.

References

[1] D.L. Marchisio, R.O. Fox, R.O. Fox, Computational Models for Polydisperse Particulate and Multiphase Systems, Vol. 9780521858489, Cambridge University Press, 2010.

[2] M.A. Watzky, E.E. Finney, R.G. Finke, Transition-metal nanocluster size vs formation time and the catalytically effective nucleus number: A mechanism-based treatment, J. Am. Chem. Soc. 130 (36) (2008).

[3] L. Bentea, M.A. Watzky, R.G. Finke, Sigmoidal nucleation and growth curves across nature fit by the Finke–Watzky model of slow continuous nucleation and autocatalytic growth: Explicit formulas for the lag and growth times plus other key insights, J. Phys. Chem. C 121 (9) (2017).

[4] Z. Wu, W. Zhou, C. Pang, W. Deng, C. Xu, X. Wang, Multifunctional chitosan-based coating with liposomes containing laurel essential oils and nanosilver for pork preservation, Food Chem. 295 (2019).

[5] S. Paul, P. Basak, R. Majumder, A. Mukherjee, J. Ghosh, S. Patra, N.K. Jana, Biochemical estimation of moringa oleifera leaf extract for synthesis of silver nanoparticle mediated drug delivery system, J. Plant Biochem. Biotechnol. 29 (1) (2020).

[6] D. Ballottin, S. Fulaz, F. Cabrini, J. Tsukamoto, N. Durán, O.L. Alves, L. Tasic, Antimicrobial textiles: Biogenic silver nanoparticles against Candida and Xanthomonas, Mater. Sci. Eng. C 75 (2017).

[7] F. Wei, X. Zhao, C. Li, X. Han, A novel strategy for water disinfection with a AgNPs/gelatin sponge filter, Environ. Sci. Pollut. Res. 25 (20) (2018).

[8] K.N. Dantas, L.R. Andrade, E. Lisboa, V.L. Santana, A.L. Santos, T.P. Mello, L.S. Sangenito, Á.S. Lima, A.T. Fricks, A.F. Begnami, A. Cano, A. Zielinska, C.M. Soares, E.B. Souto, P. Severino, Antimycotic nail polish based on humic acid-coated silver nanoparticles for onychomycosis, J. Chem. Technol. Biotechnol. 96 (8) (2021).

[9] R. Liu, J. Tang, H. Yang, W. Jin, M. Liu, S. Liu, J. Hu, In situ decoration of plasmonic silver nanoparticles on poly(vinylidene fluoride) membrane for versatile SERS detection, New J. Chem. 43 (18) (2019).

[10] X.Y. Dong, Z.W. Gao, K.F. Yang, W.Q. Zhang, L.W. Xu, Nanosilver as a new generation of silver catalysts in organic transformations for efficient synthesis of fine chemicals, Catal. Sci. Technol. 5 (5) (2015).

[11] K.S. Siddiqi, A. Husen, R.A. Rao, A review on biosynthesis of silver nanoparticles and their biocidal properties, J. Nanobiotechnology 16 (1) (2018).

[12] D. Shalom, R.C. Wootton, R.F. Winkle, B.F. Cottam, R. Vilar, A.J. deMello, C.P. Wilde, Synthesis of thiol functionalized gold nanoparticles using a continuous flow microfluidic reactor, Mater. Lett. 61 (4–5) (2007).

[13] J.B. Edel, R. Fortt, J.C. DeMello, A.J. DeMello, Microfluidic routes to the controlled production of nanoparticles, Chem. Commun. 2 (10) (2002).

[14] E.M. Chan, A.P. Alivisatos, R.A. Mathies, High-temperature microfluidic synthesis of CdSe nanocrystals in nanoliter droplets, J. Am. Chem. Soc. 127 (40) (2005).

[15] S.A. Khan, A. Günther, M.A. Schmidt, K.F. Jensen, Microfluidic synthesis of colloidal silica, Langmuir 20 (20) (2004).

[16] A. Jahn, J.E. Reiner, W.N. Vreeland, D.L. DeVoe, L.E. Locascio, M. Gaitan, Preparation of nanoparticles by continuous-flow microfluidics, J. Nanoparticle Res. 10 (2008).

[17] X.Z. Lin, A.D. Terepka, H. Yang, Synthesis of silver nanoparticles in a continuous flow tubular microreactor, Nano Lett. 4 (11) (2004).

[18] M. Rahil Hasan, N. Anzar, M. Tyagia, N. Yadav, J. Narang, Lab-on-a-chip devices-advancement in the designing of biosensors, in: Functionalized Nanomaterials Based Devices for Environmental Applications, 2021.

[19] A.D. Radadia, Microfluidics for biochemical and chemical reactions, in: Encyclopedia of Microfluidics and Nanofluidics, 2008.

[20] J.S. Kuo, D.T. Chiu, Controlling mass transport in microfluidic devices, 2011.

[21] V. Demchenko, S. Riabov, S. Kobylinskyi, L. Goncharenko, N. Rybalchenko, A. Kruk, O. Moskalenko, M. Shut, Effect of the type of reducing agents of silver ions in interpolyelectrolyte-metal complexes on the structure, morphology and properties of silver-containing nanocomposites, Sci. Rep. 10 (1) (2020).

[22] T. Zhao, R. Sun, S. Yu, Z. Zhang, L. Zhou, H. Huang, R. Du, Size-controlled preparation of silver nanoparticles by a modified polyol method, Colloids Surf. A 366 (1–3) (2010).

[23] A. Sobczak-Kupiec, D. Malina, Z. Wzorek, M. Zimowska, Influence of silver nitrate concentration on the properties of silver nanoparticles, Micro Nano Lett. 6 (8) (2011).

[24] A. Andrieux-Ledier, B. Tremblay, A. Courty, Synthesis of silver nanoparticles using different silver phosphine precursors: Formation mechanism and size control, J. Phys. Chem. C 117 (28) (2013).

[25] H. Liu, H. Zhang, J. Wang, J. Wei, Effect of temperature on the size of biosynthesized silver nanoparticle: Deep insight into microscopic kinetics analysis, Arab. J. Chem. 13 (1) (2020).

[26] M.K. Alqadi, O.A. Abo Noqtah, F.Y. Alzoubi, J. Alzouby, K. Aljarrah, PH effect on the aggregation of silver nanoparticles synthesized by chemical reduction, Mater. Sci. Poland 32 (1) (2014) 107–111.

[27] K. Nathanael, P. Pico, N.M. Kovalchuk, A.D. Lavino, M.J. Simmons, O.K. Matar, Computational modelling and microfluidics as emerging approaches to synthesis of silver nanoparticles - A review, Chem. Eng. J. 436 (2022).

[28] M.A. Watzky, R.G. Finke, Transition metal nanocluster formation kinetic and mechanistic studies. a new mechanism when hydrogen is the reductant: Slow, continuous nucleation and fast autocatalytic surface growth, J. Am. Chem. Soc. 119 (43) (1997).

[29] J.Y. Rempel, M.G. Bawendi, K.F. Jensen, Insights into the kinetics of semiconductor nanocrystal nucleation and growth, J. Am. Chem. Soc. 131 (12) (2009).

[30] S. Mozaffari, W. Li, C. Thompson, S. Ivanov, S. Seifert, B. Lee, L. Kovarik, A.M. Karim, Colloidal nanoparticle size control: Experimental and kinetic modeling investigation of the ligand-metal binding role in controlling the nucleation and growth kinetics, Nanoscale 9 (36) (2017).

[31] D.R. Handwerk, P.D. Shipman, C.B. Whitehead, S. Özkar, R.G. Finke, Mechanism-enabled population balance modeling of particle formation en route to particle average size and size distribution understanding and control, J. Am. Chem. Soc. 141 (40) (2019).

[32] J. Polte, Fundamental growth principles of colloidal metal nanoparticles - a new perspective, CrystEngComm 17 (36) (2015).

[33] S.R.K. Perala, S. Kumar, On the two-step mechanism for synthesis of transition-metal nanoparticles, Langmuir 30 (42) (2014).

[34] V.K. Lamer, R.H. Dinegar, Theory, production and mechanism of formation of monodispersed hydrosols, J. Am. Chem. Soc. 72 (11) (1950).

[35] I.M. Lifshitz, V.V. Slyozov, The kinetics of precipitation from supersaturated solid solutions, J. Phys. Chem. Solids 19 (1–2) (1961).

[36] D.R. Handwerk, P.D. Shipman, C.B. Whitehead, S. Özkar, R.G. Finke, Particle size distributions via mechanism-enabled population balance modeling, J. Phys. Chem. C 124 (8) (2020).

[37] V. Bal, R. Bandyopadhyaya, Mechanistic aspects in the formation of nano- and submicron particles in a batch and a continuous microfluidic reactor: Experiment, modeling and simulation, Chem. Eng. J. 371 (2019).

[38] V. Bal, R. Bandyopadhyaya, Generalized model for nano- and submicron particle formation in liquid phase, incorporating reaction kinetics and hydrodynamic interaction: Experiment, modeling, and simulation, J. Phys. Chem. C 122 (35) (2018).

[39] S. Kumar, S. Ganesan, Numerical simulation of nanocrystal synthesis in a microfluidic reactor, Comput. Chem. Eng. 96 (2017).

[40] T. Schikarski, M. Avila, H. Trzenschiok, A. Güldenpfennig, W. Peukert, Quantitative modeling of precipitation processes, Chem. Eng. J. 444 (2022) 136195.

[41] A.D. Lavino, M. Ferrari, A.A. Barresi, D. Marchisio, Effect of different good solvents in flash nano-precipitation via multi-scale population balance modeling-CFD coupling approach, Chem. Eng. Sci. 245 (2021).

[42] H. Liu, J. Li, D. Sun, T. Odoom-Wubah, J. Huang, Q. Li, Modeling of silver nanoparticle formation in a microreactor: Reaction kinetics coupled with population balance model and fluid dynamics, Ind. Eng. Chem. Res. 53 (11) (2014).

[43] A. Passalacqua, F. Laurent, E. Madadi-Kandjani, J.C. Heylmun, R.O. Fox, An open-source quadrature-based population balance solver for OpenFOAM, Chem. Eng. Sci. 176 (2018).

[44] K. Nathanael, S. Cheng, N.M. Kovalchuk, R. Arcucci, M.J. Simmons, Optimization of microfluidic synthesis of silver nanoparticles: a generic approach using machine learning, Chem. Eng. Res. Des. (2023).

[45] S.K. Sivaraman, I.S. Elango, S. Kumar, V. Santhanam, A green protocol for room temperature synthesis of silver nanoparticles in seconds, Current Sci. 97 (2009) 1055–1059.

[46] M.U. Rashid, M.K.H. Bhuiyan, M.E. Quayum, Synthesis of silver nano particles (Ag-NPs) and their uses for quantitative analysis of vitamin c tablets, Dhaka Univ. J. Pharm. Sci. 12 (1) (2013) 29–33.

[47] O. Kašpar, A.H. Koyuncu, A. Pittermannová, P. Ulbrich, V. Tokárová, Governing factors for preparation of silver nanoparticles using droplet-based microfluidic device, Biomed. Microdevices 21 (4) (2019) 88.

[48] I.P. Zwar, C.d.V. Trotta, A.B.S. Ziotti, M. Lima Neto, W.L. Araújo, I.S. de Melo, C.A. Ottoni, A.O. de Souza, Biosynthesis of silver nanoparticles using actinomycetes, phytotoxicity on rice seeds, and potential application in the biocontrol of phytopathogens, J. Basic Microbiol. 63 (1) (2023) 64–74.

[49] K. Ranoszek-Soliwoda, E. Tomaszewska, E. Socha, P. Krzyczmonik, A. Ignaczak, P. Orlowski, M. Krzyzowska, G. Celichowski, J. Grobelny, The role of tannic acid and sodium citrate in the synthesis of silver nanoparticles, J. Nanoparticle Res. 19 (8) (2017).

[50] A. Amirjani, D.F. Haghshenas, Modified Finke–Watzky mechanisms for the two-step nucleation and growth of silver nanoparticles, Nanotechnology 29 (50) (2018).

[51] C. Yuan, Quadrature-Based Moment Methods for Polydisperse Multiphase Flow Modeling Recommended Citation (Ph.D. thesis), Iowa State University, 2013, pp. 1–16, [Online]. Available: https://lib.dr.iastate.edu/etd/13540.

[52] R. McGraw, Description of aerosol dynamics by the quadrature method of moments, Aerosol Sci. Technol. 27 (2) (1997).
[53] J.C. Wheeler, Modified moments and gaussian quadratures, Rocky Mountain J. Math. 4 (2) (1974).
[54] V. Alopaeus, M. Laakkonen, J. Aittamaa, Solution of population balances with breakage and agglomeration by high-order moment-conserving method of classes, Chem. Eng. Sci. 61 (20) (2006).
[55] Y. Lin, K. Lee, T. Matsoukas, Solution of the population balance equation using constant-number Monte Carlo, Chem. Eng. Sci. 57 (12) (2002).
[56] M. Takesue, T. Tomura, M. Yamada, K. Hata, S. Kuwamoto, T. Yonezawa, Size of elementary clusters and process period in silver nanoparticle formation, J. Am. Chem. Soc. 133 (36) (2011).
[57] A. Passalacqua, J. Heylmun, M. Icardi, E. Madadi, P. Bachant, X. Hu, J. Weaver, OpenQBMM/OpenQBMM: OpenQBMM 6.0.0 for OpenFOAM-v2006, 2020, [Online]. Available: https://zenodo.org/record/4007235.
[58] V. John, I. Angelov, A.A. Öncül, D. Thévenin, Techniques for the reconstruction of a distribution from a finite number of its moments, Chem. Eng. Sci. 62 (11) (2007).
[59] E. Agunloye, L. Panariello, A. Gavriilidis, L. Mazzei, A model for the formation of gold nanoparticles in the citrate synthesis method, Chem. Eng. Sci. 191 (2018).
[60] H.S. Harned, C.L. Hildreth, The diffusion coefficient of silver nitrate in dilute aqueous solution at 25°, J. Am. Chem. Soc. 73 (7) (1951).
[61] T. Ung, M. Giersig, D. Dunstan, P. Mulvaney, Spectroelectrochemistry of colloidal silver, Langmuir 13 (6) (1997).
[62] J.T. Edward, Molecular volumes and the Stokes–Einstein equation, J. Chem. Educ. 47 (4) (1970).
[63] F. Moukalled, L. Mangani, M. Darwish, The Finite Volume Method in Computational Fluid Dynamics, Fluid Mechanics and its Applications, vol. 113, Springer International Publishing, Cham, 2016.
[64] C. Hirsch, Part III: The analysis of numerical schemes, in: Numerical Computation of Internal and External Flows: The Fundamentals of Computational Fluid Dynamics, Elsevier, 2007, pp. 1–656.
[65] S.V. Patankar, Numerical heat transfer and fluid flow, 1980.
[66] H.E. Sandoe, M.A. Watzky, S.A. Diaz, Experimental probes of silver metal nanoparticle formation kinetics: Comparing indirect versus more direct methods, Int. J. Chem. Kinet. 51 (11) (2019).
[67] Y. Qin, X. Ji, J. Jing, H. Liu, H. Wu, W. Yang, Size control over spherical silver nanoparticles by ascorbic acid reduction, Colloids Surf. A 372 (1–3) (2010).
[68] X. Dong, X. Ji, H. Wu, L. Zhao, J. Li, W. Yang, Shape control of silver nanoparticles by stepwise citrate reduction, J. Phys. Chem. C 113 (16) (2009).
[69] D.L. Marchisio, A.A. Barresi, R.O. Fox, Simulation of turbulent precipitation in a semi-batch taylor-couette reactor using CFD, AIChE J. 47 (3) (2001).
[70] S. Das, K. Bandyopadhyay, M.M. Ghosh, Effect of stabilizer concentration on the size of silver nanoparticles synthesized through chemical route, Inorg. Chem. Commun. 123 (2021) 108319.
[71] A. Henglein, M. Giersig, Formation of colloidal silver nanoparticles: Capping action of citrate, J. Phys. Chem. B 103 (44) (1999) 9533–9539.
[72] N.G. Bastús, F. Merkoçi, J. Piella, V. Puntes, Synthesis of highly monodisperse citrate-stabilized silver nanoparticles of up to 200 nm: Kinetic control and catalytic properties, Chem. Mater. 26 (9) (2014).
[73] L. Marciniak, M. Nowak, A. Trojanowska, B. Tylkowski, R. Jastrzab, The effect of pH on the size of silver nanoparticles obtained in the reduction reaction with citric and malic acids, Materials 13 (23) (2020).
[74] D. Bothe, C. Stemich, H.J. Warnecke, Fluid mixing in a T-shaped micro-mixer, Chem. Eng. Sci. 61 (9) (2006).
[75] K.-J. Wu, G.M. De Varine Bohan, L. Torrente-Murciano, Synthesis of narrow sized silver nanoparticles in the absence of capping ligands in helical microreactors, React. Chem. Eng. 2 (2) (2017) 116–128.
[76] S. Yoo, D.H. Nam, T.I. Singh, G. Leem, S. Lee, Effect of reducing agents on the synthesis of anisotropic gold nanoparticles, Nano Convergence 9 (1) (2022) 5.
[77] M. Iwamoto, K. Kuroda, J. Kanzow, S. Hayashi, F. Faupel, Size evolution effect of the reduction rate on the synthesis of gold nanoparticles, Adv. Powder Technol. 16 (2) (2005) 137–144.
[78] K.N. Clayton, J.W. Salameh, S.T. Wereley, T.L. Kinzer-Ursem, Physical characterization of nanoparticle size and surface modification using particle scattering diffusometry, Biomicrofluidics 10 (5) (2016).
[79] Y. Kim, B. Lee Chung, M. Ma, W.J.M. Mulder, Z.A. Fayad, O.C. Farokhzad, R. Langer, Mass production and size control of lipid–polymer hybrid nanoparticles through controlled microvortices, Nano Lett. 12 (7) (2012) 3587–3591.
[80] F.W.M. Ling, H.A. Abdulbari, C. Sim-Yee, Effect of residence time on the morphology of silica nanoparticles synthesized in a microfluidic reactor, J. Flow Chem. 12 (1) (2022) 17–30.
[81] M.T. Aljarrah, A.M. Alboull, M.S. Alharahsheh, A. Ashraf, A. Khandakar, Parametric study of gold nanoparticles synthesis under micro-continuous flow conditions, Molecules 27 (24) (2022) 8651.
[82] T. Nisisako, T. Torii, Microfluidic large-scale integration on a chip for mass production of monodisperse droplets and particles, Lab Chip 8 (2) (2008).